International Journal of Heat and Mass Transfer 52 (2009) 4731–4747

Contents lists available at ScienceDirect

International Journal of Heat and Mass Transfer

journal homepage: www.elsevier.com/locate/ijhmt

Convection film boiling on horizontal cylinders

Erik de Malmazet *, Georges Berthoud

DEN/DTN/SE2T, French Atomic Energy Commission, 17 rue des Martyrs, 38054 Grenoble Cedex 9, France

ARTICLE INFO

Article history:
Received 5 September 2008
Received in revised form 13 March 2009
Accepted 13 March 2009
Available online 22 July 2009

Keywords:
Convection film boiling
Cylinder
Two-phase boundary layer
Integral method
Vapour film stability

ABSTRACT

Free, mixed and forced convection film boiling on a horizontal cylinder in a saturated or subcooled liquid is studied theoretically using a single model based on a two-phase laminar boundary layer integral method. The vapour flow is described accurately by including the inertia and convection terms in the momentum and energy equations, in order to study convection film boiling in the cases of very high superheat. Different film boiling cases are then analysed with this model. The case of high superheat and low subcooling was first analysed by comparing the model with an experiment consisting in the quenching of wires with very high superheat: the model was able to predict the measured heat transfer from the cylinder with errors less than 30%, performing better than previous models or correlations. Additional calculations in other high superheat conditions have also been performed and compared with a model which does not include the inertia and convection terms in order to have a more quantitative idea of their effects on the heat transfers. The case of low superheat and high subcooling is then analysed by comparing the model with other forced convection experiments with cylinders at lower temperatures. By analysing different experiments, it is found that there are in fact two different forced convection film boiling sub-regimes characterised by relatively "low" or "high" heat transfers, and that the existence of these sub-regimes is probably linked with the stability of the vapour film during film boiling. The model results compare quite well with the experimental data which belong to the "stable" sub-regime but, on the other hand, the model largely underestimates the heat transfer for experimental data which belongs to the "unstable" sub-regime. Finally, the model is compared to some free convection experimental data. The model was able to predict the measured heat transfers from the cylinder with errors less than 30% both in saturated and subcooled cases.

1. Introduction

Film boiling is a heat transfer mode which occurs when there is a very high temperature difference between a liquid and the surface of a hot body. The rate of vapourisation of the liquid is so high that a continuous vapour sheet entirely encloses the hot body, preventing direct contact between the liquid and the hot surface. In this configuration, the heat transfer is relatively low compared to other heat transfer regimes such as nucleate or transition boiling due to the presence of the vapour film insulating the hot body.

The film boiling regime is of important concern in nuclear severe accident analysis in the case of a core meltdown. The fast interaction between the very high temperature drops or particles of melt and the cooler liquid coolant may lead to what is called a vapour explosion, which is generated by a very intensive vapourisation of the coolant. In order to evaluate the total amount of coolant vapour generated and the heat transferred to the liquid coolant, the mechanisms of mass and heat transfer between each hot drop or particle and the coolant at various temperatures, pressures and relative velocities must be understood.

However, previously developed models for forced convection film boiling may not be suitable to study physical phenomena with such high temperatures. This is due to the common assumption that heat transfer in film boiling is mainly due to conduction through the vapour film, an assumption that is made for simplicity reasons because it allows the use of a linear temperature profile in the vapour film. But in the cases of very high superheat and low subcooling, this assumption is probably no more valid. Moreover, some previous models developed for free convection on horizontal cylinders [15] or on vertical flat [16] plates included the convective and inertial terms in the vapour flow in order to better predict some experimental data corresponding to film boiling of cryogenic fluids.

Also, in the opposite case of low superheat and high subcooling, previous forced convection film boiling models for horizontal cylinders or spheres do not give satisfactory results because they always seem to underestimate the heat transfer at the body surface.

In this paper, a theoretical analysis of the convection film boiling past an horizontal cylinder based on a two-phase laminar boundary layer model is first described which is similar to the

* Corresponding author. Tel.: +33 4 38 78 22 81.
E-mail address: erik.demalmazet@cea.fr (E. de Malmazet).

0017-9310/$ - see front matter © 2009 Published by Elsevier Ltd.
doi:10.1016/j.ijheatmasstransfer.2009.03.065

Nomenclature

C_p	heat capacity at constant pressure
d	cylinder diameter
Fr	Froude number, $Fr = u_\infty^2/gr$
g	gravity acceleration
h_{LV}	latent heat of evaporation
k	thermal conductivity
$\dot{m}$	rate of vapourisation
$\dot{M}$	dimensionless rate of vapourisation, $\dot{M} = \dot{m}/\dot{m}^*$
P	pressure
Pr	Prandtl number, $Pr = \nu/\alpha$
r	cylinder radius
Re	Reynolds number, $Re = u_\infty r/\nu_L$
T	temperature
ΔT_{sub}	liquid subcooling, $\Delta T_{sub} = T_{sat} - T_\infty$
ΔT_{sup}	surface superheat: $\Delta T_{sup} = T_s - T_{sat}$
u	tangential velocity
U	dimensionless tangential velocity, $U = u/u_\infty$
v	radial velocity
W	dimensionless tangential velocity, $W = u/u_e$
x	distance from front stagnation point
y	distance from cylinder surface
α	thermal diffusivity
δ_V	vapour film thickness
Δ_V	dimensionless vapour film thickness, $\Delta_V = \delta_V/\delta_V^*$
δ_{Lm}	liquid momentum boundary layer thickness
Δ_{Lm}	dimensionless liquid momentum boundary layer thickness, $\Delta_{Lm} = \delta_{Lm}/\delta_{Lm}^*$
δ_{Lt}	liquid thermal boundary layer thickness
Δ_{Lt}	dimensionless liquid thermal boundary layer thickness, $\Delta_{Lt} = \delta_{Lt}/\delta_{Lt}^*$
μ	dynamic viscosity
ν	kinematic viscosity
ρ	density
θ	angle from front stagnation point

Subscripts

∞	free stream
e	external flow (liquid potential flow outside the liquid boundary layer)
i	vapour–liquid interface
L	liquid
m	momentum
s	cylinder surface
sat	saturation
t	thermal
V	vapour

Superscript

*	characteristic value

Shigeshi and Ito models (see [1,2]) but includes the convection and the inertia terms to fully describe the flow inside the vapour film. This model is suitable for describing natural, mixed or forced convection film boiling in the cases of high liquid subcooling, low liquid subcooling and also saturated liquid. The model is then compared to some experimental data and to other theoretical models.

2. Model description

Fig. 1 shows the configuration of convection film boiling past a horizontal cylinder. We consider the problem of a hot horizontal cylinder of radius r and of constant and uniform temperature T_s past an upward liquid flow of velocity u_∞, temperature T_∞ and pressure P_∞. The gravity is not neglected in order to take into account buoyancy effect at small velocities. The problem is studied using a system of coordinates where x represents the distance from the forward stagnation point and y the distance from the surface. The forced convection film boiling model is based on a steady state two-phase boundary layer theory approach where the flow inside the vapour film is described as a boundary layer, as well as the adjacent liquid flow. δ_V, δ_{Lm} and δ_{Lt} are the thicknesses of the vapour film, the liquid momentum boundary layer and the liquid thermal boundary layer, the boundaries of which are located, respectively, at the distances $y_i = \delta_V$, $y_m = \delta_V + \delta_{Lm}$ and $y_t = \delta_V + \delta_{Lt}$ from the surface. The two-phase boundary layer approximation is valid if $y_m/r \ll 1$ and $y_t/r \ll 1$. We also make the following assumptions:

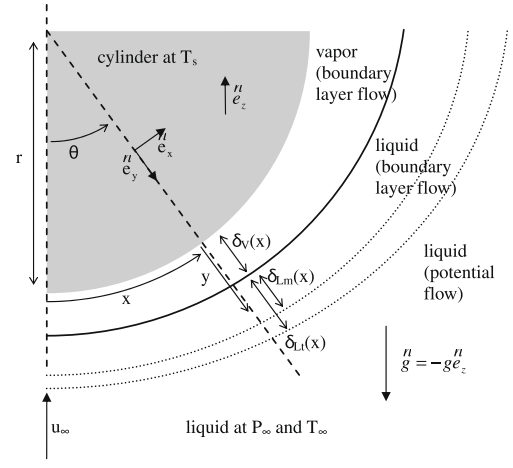

Fig. 1. Physical model, flow configuration and system of coordinates.

1. The flow in the vapour film and in the liquid boundary layer is laminar and incompressible.
2. The flow outside the liquid boundary layer is described by potential flow over a cylinder.
3. The pressure and temperature differences at the interface due to surface tension and thermodynamic non-equilibrium are neglected.
4. Due to the boundary layer approximation, the pressure along the y axis is constant in the vapour and liquid phases. Using hypothesis 3, this implies that the pressure in the liquid and vapour phases is equal to the pressure outside the liquid boundary layer.
5. The variation of the saturation temperature at the interface corresponding to the variation of the pressure in the free stream is neglected. The constant saturation temperature, T_{sat}, is the one corresponding to P_∞.
6. The physical properties of the liquid and the vapour are constant. The physical properties are evaluated at $(T_{sat} + T_\infty)/2$ for the liquid and at $(T_s + T_{sat})/2$ for the vapour.
7. Radiation heat transfer is not considered.

Based on these assumptions, the flow around the cylinder is described by the following equations:

– Outside the liquid boundary layer (tangential velocity and pressure gradient equations for potential flow past a cylinder):

$$u_e = 2u_\infty \sin(\theta) = 2u_\infty \sin(x/r) \tag{1}$$

$$\frac{dP}{dx} = -\rho_L u_e \frac{du_e}{dx} - \rho_L g \sin(\theta) = -\rho_L u_e \frac{du_e}{dx} - \rho_L g \sin(x/r) \tag{2}$$

– Inside the liquid boundary layer (mass, momentum and energy equations):

$$\frac{\partial v_L}{\partial y} + \frac{\partial u_L}{\partial x} = 0 \tag{3}$$

$$v_L \frac{\partial u_L}{\partial y} + u_L \frac{\partial u_L}{\partial x} = u_e \frac{du_e}{dx} + \nu_L \frac{\partial^2 u_L}{\partial y^2} \tag{4}$$

$$v_L \frac{\partial T_L}{\partial y} + u_L \frac{\partial T_L}{\partial x} = \alpha_L \frac{\partial^2 T_L}{\partial y^2} \tag{5}$$

– Inside the vapour film (mass, momentum and energy equations):

$$\frac{\partial v_V}{\partial y} + \frac{\partial u_V}{\partial x} = 0 \tag{6}$$

$$v_V \frac{\partial u_V}{\partial y} + u_V \frac{\partial u_V}{\partial x} = \frac{(\rho_L - \rho_V)}{\rho_V} g \sin(\theta) + \frac{\rho_L}{\rho_V} u_e \frac{du_e}{dx} + \nu_V \frac{\partial^2 u_V}{\partial y^2} \tag{7}$$

$$v_V \frac{\partial T_V}{\partial y} + u_V \frac{\partial T_V}{\partial x} = \alpha_V \frac{\partial^2 T_V}{\partial y^2} \tag{8}$$

– At the liquid–vapour interface (tangential velocity, mass, momentum and energy interfacial balance equations):

$$u_L = u_V \hat{=} u_i \hat{=} W_i u_e \tag{9}$$

$$\rho_L \left(u_L \frac{dy_i}{dx} - v_L \right) = \rho_V \left(u_V \frac{dy_i}{dx} - v_V \right) = \dot{m} \tag{10}$$

$$\mu_L \frac{\partial u_L}{\partial y} = \mu_V \frac{\partial u_V}{\partial y} \tag{11}$$

$$h_{LV} \dot{m} = -k_V \frac{\partial T_V}{\partial y} + k_L \frac{\partial T_L}{\partial y} \tag{12}$$

In Eq. (9), u_i and W_i represent, respectively, the dimensional and dimensionless tangential interfacial velocity.

The boundary layer model that will be described in this paper is based on an integral method, which was already used in similar previously developed models [1–3]. It basically consists in integrating the liquid and vapour equations along the y axis by using polynomial velocity and temperature profiles in the boundary layers, thus eliminating the y dependent variables. In the previous models, by neglecting the inertia and convection terms in the vapour flow, it was possible to obtain an expression of $\delta_{Lm}(x)$ as a function of the variables $\delta_V(x)$, $\delta_{Lt}(x)$ and the interfacial dimensionless tangential velocity $W_i(x)$, and then a linear system of three ordinary differential equations verified by the three previous variables which was solved numerically. However, if inertia and convection terms are added, it is still possible to find a simple numerical solution of the problem using an integral method by just introducing an additional variable which is the rate of vapourisation $\dot{m}(x)$. We show that a linear system of five ordinary differential equations verified by the five variables can be obtained. This is the major improvement of the present model: there is no need to neglect terms in the vapour flow for simplicity reasons, because the numerical solution of this model is as simple as the previous ones. The model is now described.

For a given value of x, we assume polynomial functions of y for $u_L(y,x)$, $u_V(y,x)$, $T_L(y,x)$ and $T_V(y,x)$ and integrate the boundary layer equations with respect to y. In order to take into account the inertia terms in the vapour momentum equation and the convection terms in the vapour energy equation, polynomial functions of at least order 3 are needed for u_V and T_V. For u_L and T_L, only quadratic functions of y are used. We assume the following expressions for u_L, $T_L u_V$ and T_V:

$$u_L = u_e \left(A_{0L} + A_{1L} \left(\frac{y - y_i}{\delta_{Lm}} \right) + A_{2L} \left(\frac{y - y_i}{\delta_{Lm}} \right)^2 \right) \hat{=} u_e W_L \tag{13}$$

$$T_L - T_\infty = (T_{sat} - T_\infty) \left(B_{0L} + B_{1L} \left(\frac{y - y_i}{\delta_{Lt}} \right) + B_{2L} \left(\frac{y - y_i}{\delta_{Lt}} \right)^2 \right) \tag{14}$$

$$u_V = u_e \left(A_{0V} + A_{1V} \left(\frac{y}{\delta_V} \right) + A_{2V} \left(\frac{y}{\delta_V} \right)^2 + A_{3V} \left(\frac{y}{\delta_V} \right)^3 \right) \hat{=} u_e W_V \tag{15}$$

$$T_V - T_{sat} = (T_s - T_{sat}) \left(B_{0V} + B_{1V} \left(\frac{y}{\delta_V} \right) + B_{2V} \left(\frac{y}{\delta_V} \right)^2 + B_3 V \left(\frac{y}{\delta_V} \right)^3 \right) \tag{16}$$

The coefficients are calculated using the following boundary conditions:

- Liquid tangential velocity u_L:

$$u_L(y_i, x) = u_i(x) \tag{17}$$

$$u_L(y_m, x) = u_e(x) \tag{18}$$

$$\frac{\partial u_L}{\partial y}(y_m, x) = 0 \tag{19}$$

- Liquid temperature T_L:

$$T_L(y_i, x) = T_{sat} \tag{20}$$

$$T_L(y_t, x) = T_\infty \tag{21}$$

$$\frac{\partial T_L}{\partial y}(y_t, x) = 0 \tag{22}$$

- Vapour tangential velocity u_V:

$$u_V(0, x) = 0 \tag{23}$$

$$\frac{\mu_V}{\rho_V} \frac{\partial^2 u_V}{\partial y^2}(0, x) = -\left(\frac{\rho_L - \rho_V}{\rho_V} \right) g \sin(x/r) - \frac{\rho_L}{\rho_V} u_e(x) \frac{du_e}{dx}(x) \tag{24}$$

$$u_V(y_i, x) = u_i(x) \tag{25}$$

$$\mu_V \frac{\partial u_V}{\partial y}(y_i, x) = \mu_L \frac{\partial u_L}{\partial y}(y_i, x) \tag{11}$$

- Vapour temperature T_V:

$$T_V(0, x) = T_s \tag{26}$$

$$\alpha_V \frac{\partial^2 T_V}{\partial y^2}(0, x) = 0 \tag{27}$$

$$T_V(y_i, x) = T_{sat} \tag{28}$$

$$k_V \frac{\partial T_V}{\partial y}(y_i, x) = -\dot{m} h_{LV} + k_L \frac{\partial T_L}{\partial y}(y_i, x) \tag{12}$$

These boundary conditions lead to the following expressions for the coefficients:

$$A_{0L} = W_i \tag{29}$$

$$A_{1L} = -2(W_i - 1) \tag{30}$$

$$A_{2L} = W_i - 1 \tag{31}$$

$$B_0 L = 1 \tag{32}$$

$$B_{1L} = -2 \tag{33}$$
$$B_{2L} = 1 \tag{34}$$
$$A_{0V} = 0 \tag{35}$$
$$A_{1V} = \frac{3}{2}W_i + \frac{1}{4}F_V + A_V \tag{36}$$
$$A_{2V} = -\frac{1}{2}F_V \tag{37}$$
$$A_{3V} = -\frac{1}{2}W_i + \frac{1}{4}F_V - A_V \tag{38}$$

with

$$F_V = \frac{\rho_L}{\mu_V}\delta_V^2\left(\frac{du_e}{dx} + \frac{1}{2}\left(\frac{\rho_L - \rho_V}{\rho_L}\right)\frac{g}{u_\infty}\right) \quad \text{and} \quad A_V = \frac{\mu_L}{\mu_V}(W_i - 1)\frac{\delta_V}{\delta_{Lm}}$$

$$B_{0V} = 1 \tag{39}$$
$$B_{1V} = -\frac{3}{2} + \frac{1}{2}B_V \tag{40}$$
$$B_{2V} = 0 \tag{41}$$
$$B_{3V} = \frac{1}{2} - \frac{1}{2}B_V \tag{42}$$

with

$$B_V = \frac{h_{LV}}{k_V(T_s - T_{sat})}\delta_V\dot{m} + 2\frac{k_L(T_{sat} - T_\infty)}{k_V(T_s - T_{sat})}\frac{\delta_V}{\delta_{Lt}}$$

Now the integration of the boundary layer equations is possible. This is done by first integrating the liquid and vapour mass equations. Integrating (3) over the liquid momentum and energy boundary layers, and integrating (6) over the vapour film gives:

$$v_L(y_m, x) = -\frac{d}{dx}\int_{y_i}^{y_m} u_L(y,x)dy + u_L(y_m,x)\frac{dy_m}{dx} - \frac{\dot{m}}{\rho_L} \tag{3i$_m$}$$

$$v_L(y_t, x) = -\frac{d}{dx}\int_{y_i}^{y_t} u_L(y,x)dy + u_L(y_t,x)\frac{dy_t}{dx} - \frac{\dot{m}}{\rho_L} \tag{3i$_t$}$$

$$v_V(y_i, x) = -\frac{d}{dx}\int_{0}^{y_i} u_V(y,x)dy + u_V(y_i,x)\frac{dy_i}{dx} \tag{6i}$$

Using Eqs. (3i$_m$) and (3i$_i$) we integrate the liquid momentum and energy equations, respectively, over the liquid momentum and energy boundary layers, and using Eq. (6i) we integrate the vapour momentum and energy equations over the vapour film thickness. This is done by using auxiliary dimensionless functions called F_{1L}, F_{2L}, G_L, F_{1V}, F_{2V} and G_V defined as follows:

$$\int_{y_i}^{y_m}(u_e - u_L)dy \hat{=} u_e\delta_{Lm}F_{1L} \tag{43}$$
$$\int_{y_i}^{y_m}u_L(u_e - u_L)dy \hat{=} u_e^2\delta_{Lm}F_{2L} \tag{44}$$
$$\int_{y_i}^{y_m}u_L(T_L - T_\infty)dy \hat{=} u_e(T_{sat} - T_\infty)\delta_{Lt}G_L \tag{45}$$
$$\int_{0}^{y_i}u_V\,dy \hat{=} u_e\delta_V F_{1V} \tag{46}$$
$$\int_{0}^{y_i}u_V^2\,dy \hat{=} u_e^2\delta_V F_{2V} \tag{47}$$
$$\int_{0}^{y_i}u_V(T_V - T_{sat})dy \hat{=} u_e(T_s - T_{sat})\delta_V G_V \tag{48}$$

Using these functions and integrating the boundary layer equations, we get:

$$u_eF_{2L}\frac{d\delta_{Lm}}{dx} + u_e\delta_{Lm}\frac{dF_{2L}}{dx} = (W_i - 1)\frac{\dot{m}}{\rho_L} - 2F_{2L}\delta_{Lm}\frac{du_e}{dx} - \delta_{Lm}F_{1L}\frac{du_e}{dx} + \frac{v_L}{\delta_{Lm}}A_{1L} \tag{4i}$$

$$u_eG_L\frac{d\delta_{Lt}}{dx} + u_e\delta_{Lt}\frac{dG_L}{dx} = -\frac{\dot{m}}{\rho_L} - \delta_{Lt}G_L\frac{du_e}{dx} - \frac{\alpha_L}{\delta_{Lt}}B_{1L} \tag{5i}$$

$$u_eF_{2V}\frac{d\delta_V}{dx} + u_e\delta_V\frac{dF_{2V}}{dx} = W_i\frac{\dot{m}}{\rho_V} - 2\delta_VF_{2V}\frac{du_e}{dx} + \frac{\rho_L}{\rho_V}\frac{du_e}{dx}\delta_V + \frac{1}{2}\frac{\rho_L - \rho_V}{\rho_V}\frac{g\delta_V}{u_\infty} + \frac{v_V}{\delta_V}(2A_{2V} + 3A_{3V}) \tag{7i}$$

$$u_eG_V\frac{d\delta_V}{dx} + u_e\delta_V\frac{dG_V}{dx} = -\delta_VG_V\frac{du_e}{dx} + \frac{\alpha_V}{\delta_V}(2B_{2V} + 3B_{3V}) \tag{8i}$$

The auxiliary functions, as well as the polynomial coefficients, can be expressed as functions of x and of the five variables W_i, δ_V, δ_{Lm}, δ_{Lt} and $\dot{m}$. The derivatives of the auxiliary functions can be expressed as functions of the previous variables and their derivatives. For example, we can rewrite Eq. (4i) using the following expression for the derivative of $F_{2L}(x, W_i(x), \delta_V(x), \delta_{Lm}(x), \delta_{Lt}(x), \dot{m}(x))$:

$$\frac{dF_{2L}}{dx} = \frac{\partial F_{2L}}{\partial x} + \frac{\partial F_{2L}}{\partial W_i}\frac{dW_i}{dx} + \ldots + \frac{\partial F_{2L}}{\partial \dot{m}}\frac{d\dot{m}}{dx} \tag{49}$$

In order to obtain a linear system of five ordinary differential equations verified by the five variables W_i, δ_V, δ_{Lm}, δ_{Lt} and $\dot{m}$, we need an extra differential equation. This is possible by rewriting the integrated vapour mass equation (6i) using (10) and (42) in the following form:

$$u_eF_{1V}\frac{d\delta_V}{dx} + u_e\delta_V\frac{dF_{1V}}{dx} = \frac{\dot{m}}{\rho_V} - \delta_VF_{1V}\frac{du_e}{dx} \tag{6i$'$}$$

Eqs. (4i), (5i), (7i), (8i) and (6i$'$) form a linear system of five ordinary differential equations which can easily be solved numerically. At $x = 0$, the system is also defined if we use a symmetry argument: due to the symmetry of the problem, the derivative of the five variables with respect to x at the forward stagnation point is 0 (this means that the right member of each equation divided by u_e converges to 0 when $x \to 0$). The initial values of W_i, δ_V, δ_{Lm}, δ_{Lt} and $\dot{m}$ are calculated by simply writing Eqs. (4i), (5i), (7i), (8i) and (6i$'$) at $x = 0$, where the left member of each of the five equations is equal to 0 because $u_e(0) = 0$. This leads to a system of five equations verified by the initial values of the five variables, $W_i(0)$, $\delta_V(0)$, $\delta_{Lm}(0)$, $\delta_{Lt}(0)$ and $\dot{m}(0)$, which is also solved numerically.

Instead of directly solving the previous differential system, it is better to write it in a fully dimensionless form using. First we evaluate the characteristic values of the five main variables W_i, δ_V, δ_{Lm}, δ_{Lt} and $\dot{m}$, which will be defined here as W_i^*, δ_V^*, δ_{Lm}^*, δ_{Lt}^* and $\dot{m}^*$, and which depend on the studied flow configuration. This is done by using the following characteristic values for the other variables: $u_e^* = u_\infty$ and $x^* = r$. It is also interesting to use the characteristic value of the dimensionless tangential vapour velocity $W_V = u_V/u_e$, which is obtained using the integrated vapour mass equation (6i) rewritten in the following form:

$$\frac{\dot{m}}{\rho_V} = \frac{d}{dx}\int_0^{y_i}u_V(y,x)dy \tag{6i$''$}$$

From (6i$''$) we get:

$$W_V^* = \frac{\dot{m}^*r}{\rho_V\delta_V^*u_\infty} \tag{50}$$

We then define the dimensionless variables $W_i' = W_i/W_i^*$, $\Delta_V = \delta_V/\delta_V^*$, $\Delta_{Lm} = \delta_{Lm}/\delta_{Lm}^*$, $\Delta_{Lt} = \delta_{Lt}/\delta_{Lt}^*$ and $\dot{M} = \dot{m}/\dot{m}^*$. By also using the dimensionless variables $X = x/r = \theta$ and $U_e = u_e/u_\infty = 2\sin(X) = 2\sin(\theta)$ and the dimensionless numbers $Re = u_\infty r/\nu_L$, $Pr_L = \nu_L/\alpha_L$ and $Fr = u_\infty^2/gr$ (respectively the Reynolds, the liquid Prandtl and the Froude numbers), the differential system can be written in the following dimensionless form, for $\theta > 0$:

$$F_{2L}\frac{d\Delta_{Lm}}{d\theta}+\Delta_{Lm}\frac{dF_{2L}}{d\theta}=\frac{1}{U_e}\left(\frac{\dot m^*\delta^*_{Lm}}{\mu_L}\frac{r^2}{Re\,\delta^{*2}_{Lm}}(W^*_iW'_i-1)\dot M -(2F_{2L}+F_{1L})\Delta_{Lm}\frac{dU_e}{d\theta}+\frac{r^2}{Re\,\delta^{*2}_{Lm}}\frac{A_{1L}}{\Delta_{Lm}}\right) \tag{4I}$$

$$G_L\frac{d\Delta_{Lt}}{d\theta}+\Delta_{Lt}\frac{dG_L}{d\theta}=-\frac{1}{U_e}\left(\frac{\dot m^*\delta^*_{Lt}}{\rho_L\alpha_L}\frac{r^2}{Pr_L\,Re\,\delta^{*2}_{Lt}}\dot M+\Delta_{Lt}G_L\frac{dUe}{d\theta} +\frac{r^2}{Pr_L\,Re\,\delta^{*2}_{Lt}}\frac{B_{1L}}{\Delta_{Lt}}\right) \tag{5I}$$

$$\frac{1}{W^*_V}\left(F_{1V}\frac{d\Delta_V}{d\theta}+\Delta_V\frac{dF_{1V}}{d\theta}\right)=\frac{1}{U_e}\left(\dot M-\frac{1}{W^*_V}\Delta_VF_{1V}\frac{dU_e}{d\theta}\right) \tag{6I}$$

$$\frac{1}{W^{*2}_V}\left(F_{2V}\frac{d\Delta_V}{d\theta}+\Delta_V\frac{dF_{2V}}{d\theta}\right)=\frac{1}{U_e}\left(\frac{1}{W^*_V}W^*_iW'_i\dot M-\frac{2}{W^{*2}_V}F_{2V}\Delta_V\frac{dU_e}{d\theta} +\frac{1}{W^{*2}_V}\frac{\rho_L}{\rho_V}\Delta_V\frac{dU_e}{d\theta}+\frac{1}{2W^{*2}_V}\frac{\rho_L-\rho_V}{\rho_V}\frac{1}{Fr}\Delta_V +\frac{\mu_V}{\delta^*_V\dot m^*}\frac{1}{W^*_V}\frac{1}{\Delta_V}(2A_{2V}+3A_{3V})\right) \tag{7I}$$

$$\frac{1}{W^*_V}\left(G_V\frac{d\Delta_V}{d\theta}+\Delta_V\frac{dG_V}{d\theta}\right)=\frac{1}{U_e}\left(-\frac{1}{W^*_V}\Delta_VG_V\frac{dU_e}{d\theta} +\frac{\alpha_V\rho_V}{\delta^*_V\dot m^*}\frac{1}{\Delta_V}(2B_{2V}+3B_{3V})\right) \tag{8I}$$

This is the most general form of the system which is solved numerically. An example of scaling analysis used for forced convection will be given here. In the case of forced or mixed convection in which Fr is not $\ll 1$, W^*_i is assumed to be of order 1 ($W^*_i=1$), so we have $W'_i=W_i$. In fact, in most of the cases studied in this paper, the calculated vapour and liquid tangential velocities showed that the vapour moves faster than the boundary layer liquid, which in turn moves faster than the liquid in potential flow, meaning that $W_i>1$. On the other hand, we never get very high values for W_i, and the calculated values presented in this paper for forced convection were always such as $W_i<3$. For δ^*_{Lm}, the same characteristic value as in case of liquid single phase forced convection over a cylinder is used:

$$\delta^*_{Lm}=rRe^{-1/2} \tag{51}$$

δ^*_{Lt} is calculated using the liquid mass and energy equations (3) and (5). In both the cases $\delta^*_{Lt}\ll\delta^*_{Lm}$ or $\delta^*_{Lt}\gg\delta^*_{Lm}$, we have $W_i\sim 1$ and $u_L\sim u_\infty$. This implies that in both cases we have the same characteristic value for v_L, which is $(\delta^*_{Lt}/r)u_\infty$. This finally gives for δ^*_{Lt}:

$$\delta^*_{Lt}=rPr_L^{-1/2}Re^{-1/2} \tag{52}$$

To evaluate δ^*_V and $\dot m^*$, we first use the momentum balance (11) at the liquid–vapour interface. Using (11) and (50) yields:

$$\dot m^*=\frac{\mu_L\rho_Vu_\infty}{\mu_Vr}\frac{\delta^{*2}_V}{\delta^*_{Lm}} \tag{53}$$

Two extreme cases, named case 1 and case 2, may be distinguished using the energy balance equation at the liquid–vapour interface (12). In case 1, there is low superheat and high subcooling. Most of the heat received by the interface from the vapour side is used to heat the liquid and we have:

$$h_{LV}\dot m(x)\ll -k_V\frac{\partial T_V}{\partial y}(y_i,x)\ \Rightarrow\ -k_V\frac{\partial T_V}{\partial y}(y_i,x)\approx -k_L\frac{\partial T_L}{\partial y}(y_i,x)$$

This condition gives an expression of δ^*_V as a function of δ^*_{Lt} in case 1:

$$\delta^*_{Vc1}=\frac{k_V(T_s-T_{sat})}{k_L(T_{sat}-T_\infty)}\delta^*_{Lt} \tag{54}$$

$\dot m^*_{c1}$ is then calculated using (53).

Case 2 corresponds to situations where there is high superheat and low subcooling. Most of the heat received by the interface from the vapour side is used to vapourise the liquid and we have:

$$-k_L\frac{\partial T_L}{\partial y}(y_i,x)\ll -k_V\frac{\partial T_V}{\partial y}(y_i,x)\Rightarrow -k_V\frac{\partial T_V}{\partial y}(y_i,x)\approx h_{LV}\dot m(x)$$

This condition gives a second equation verified by δ^*_V and $\dot m^*$ for the case 2:

$$\dot m^*_{c2}=\frac{k_V(T_s-T_{sat})}{h_{LV}\delta^*_{Vc1}} \tag{55}$$

And we deduce the values of δ^*_V and $\dot m^*$ for case 2 by the following relations:

$$\delta^{*3}_{Vc2}=\frac{\mu_V}{\mu_L}\frac{rk_V(T_s-T_{sat})}{u_\infty\rho_Vh_{LV}}\delta^*_{Lm} \tag{56}$$

$$\dot m^*_{c2}=\frac{k_V(T_s-T_{sat})}{h_{LV}\delta^*_{Vc2}} \tag{57}$$

3. Forced convection film boiling for "high" surface superheat

In this part, the model results will first be compared to the results of an experimental apparatus called TREPAM, which description, results and analysis are detailed in [4]. This experiment consists in the quenching of thin wires preheated at very high temperatures (wire diameters from 10 to 250 μm and wire initial temperatures from 1350 to 2900 K) immersed into water at various pressures (from 1 to 210 bar), temperatures (water subcooling from 0 to 350 K) and at different velocities (from 0.2 to 46 m s^{-1}), in order to investigate heat transfer between small hot particles and a cold liquid during a vapour explosion. The main feature of TREPAM compared to many other existing quenching experiments is that it investigates convection film boiling within parameters much closer to the physical conditions of a vapour explosion, i.e. at much higher temperatures and pressures. In such physical conditions, it is expected that including the influence of the inertia and convection terms in the description of the vapour flow is necessary to properly evaluate the heat transfer from the hot wire.

The TREPAM tests can be modelled using the present model because although the temperatures reached are very high (>2000 °C), the radiation heat transfer is minimised by using tungsten wires. Due to the low emissivity of tungsten, the radiative contribution is at maximum 5% of the measured heat flux. Also, the pressure jump at the interface due to surface tension is always negligible in the TREPAM tests, even when considering the thinner wires at the lower pressures. For example, for one test where $d=8.61$ μm and $P_\infty=1$ bar, the pressure jump due to surface tension is $\Delta P=2\sigma/d\approx 0.137$ bar, only 13.7% of P_∞. In fact, if only the relevant tests are considered (the tests where the boundary layer approximation is valid), ΔP is much smaller, usually less than 1% of P_∞.

3.1. Typical TREPAM test run and typical model calculation

In each test run, a water filled tank is moved upward at a given constant speed in order to immerse a stationary preheated hot wire. By continuously measuring the temperature dependent electric resistance of the wire during the quenching, it is possible to evaluate its temperature temporal evolution $T_s(t)$, and thus the instantaneous surface averaged heat flux $q_{exp}(t)$ evacuated from the wire and the instantaneous heat transfer coefficient $h_{exp}(t)$ defined as $h_{exp}(t)=q_{exp}(t)/(T_s(t)-T_{sat})$. Typically, during each test run (see [4]), the heat flux $q_{exp}(t)$ will rapidly rise when the wire begins its immersion reaching a maximum value $q_{peak,exp}$ shortly after its full immersion at $t=t_{peak}$, and then will begin to decrease slowly,

almost linearly, as the wire temperature decreases. We consider that in this region, the film boiling heat transfer can be studied using a quasi-steady approach, which is suitable for the present model. In practice, for each test, $q_{peak,exp}$ will be compared to the value $q_{peak,theo}$ calculated with the present model using the wire temperature $T_s(t_{peak})$.

For each model calculation, there is first a simple scaling analysis in order to evaluate characteristic values for each variable, which "initial" values at the forward stagnation point are calculated. The dimensionless differential system is then integrated from $\theta = 0$ to $\theta = \theta_{div}$ at which point the calculation diverges. There are basically two kinds of calculation divergences, which depend on the flow configuration. In the cases of high wire superheats and low water subcoolings, the calculation diverges shortly after vapour flow separation occurs. In the cases of low superheats and high subcoolings, there is no vapour flow separation, but the calculation diverges because the quadratic liquid tangential velocity profile becomes flat, which happens when $W_i \to 1$. In these cases, the calculation divergence has no physical meaning: a higher order velocity profile would enable the calculation to go further and diverge only at the vapour flow separation point. Typically, θ_{div} is close to $\pi/2$ in forced convection film boiling, and gets progressively closer to π when the velocity decreases and approaches the mixed and then the natural convection velocity regimes.

Because according to calculation the vapour film thickness dramatically increases close to the vapour flow separation point, we suppose that it physically corresponds to the formation of a large vapour wake behind the cylinder. In this region, we suppose that heat transfer from the surface is negligible compared to the front region covered with the thin vapour layer. Therefore, in order to calculate the surface averaged heat flux q, the total linear heat flux Q is first calculated by integrating the local superficial heat flux from $\theta = 0$ to $\theta = \theta_{div}$ and then divided by the total area of the cylinder per length unit, which is $2\pi r$.

3.2. Comparison of the model results with the TREPAM tests and other models

Before showing the model results for the TREPAM tests, it is necessary to remind the results analysis given in [4]. By undertaking a scaling analysis for forced convection film boiling, two extreme cases were identified: the case where most of the heat lost by the wire is used to heat the liquid (referred as "case 1") and the case where most of this heat is used to vapourise the liquid (referred as "case 2"). The TREPAM tests which did not fit in one of these categories were classified as "intermediate case" tests. It was then possible to classify all the tests using two dimensionless numbers based on the previous analysis. Among the case 1 tests, two sub-cases were identified based on the heat coefficient h_{exp} behaviour during the quasi-steady regime of the wire quenching: the sub-case where $h_{exp}(t)$ will rise (case 1.1) and the sub-case where $h_{exp}(t)$ will decrease (case 1.2). The TREPAM tests classification is given in Table 1.

The main results of the model are given in Table 2. When comparing $q_{peak,exp}$ and $q_{\mathrm{peak,th}}$, we see that the model results are quite good, because in most of the tests, $q_{peak,exp}$ is predicted with a relative error smaller than 30%. In general, the model predicts a smaller heat flux than the observed one, which is coherent with the model hypothesis that heat transfer at the back of the cylinder is negligible. The few tests in which $q_{peak,exp}$ is not accurately predicted, as for example T27, T29, T58 or T63, correspond to the tests with the lower speeds and the smaller diameters. In these tests, the Reynolds number Re is very small, meaning that the boundary layer approximation ($y_m/r \ll 1$ and $y_t/r \ll 1$) is not valid. Sometimes, even if Re is not very small, the vapourisation rate is so strong that it produces a very thick vapour film, meaning that the approximation $y_i/r \ll 1$ is not valid. The calculated values of δ_V, δ_{Lm} and δ_{Lt} at the forward stagnation point shown in Table 2 confirm this analysis. In conclusion, it can be said that the agreement of the model with the experimental results is quite good, considering the variety of physical parameters (pressure, velocity, saturated tests, highly subcooled tests) that have been tested.

The theoretical values of q_{peak} calculated with two other models are also given in Table 2. The first one is the Shigeshi and Ito model (SI model) which consists in fact in two different models corre-

Table 1
TREPAM tests classification. No. 3–17: case 1.1 tests, no. 25–5: case1.2 tests, no. 45–69: intermediate case tests, no. 72–74: case 2 tests.

Test no.	P_∞ (bar)	d (μm)	u_∞ (m s^{-1})	ΔT_{sup} (K)	ΔT_{sub} (K)	$q_{peak,exp}$ (MW m^{-2})
3	1.0	94.59	1.7	1785	80	17.5
28	1.0	8.95	2.2	1727	80	35.0
29	1.0	8.61	2.2	1627	80	36.0
27	1.0	8.77	2.2	1427	80	26.0
57	1.2	232.80	0.2	972	85	5.4
59	1.2	242.11	0.2	1472	81	6.8
40	1.2	230.91	2.0	1317	88	11.0
53	1.2	100.00	2.0	1401	84	13.9
54	1.2	95.78	2.0	1922	85	18.0
61	1.2	46.63	0.2	1922	75	16.0
60	1.2	47.50	0.2	1252	82	8.7
62	1.2	45.01	0.2	1007	40	6.0
48	1.2	37.60	2.0	1752	87	24.0
36	1.2	46.61	2.0	1145	81	16.1
65	1.2	23.45	0.2	1422	77	14.5
64	1.2	23.81	0.2	898	77	10.9
71	10.0	94.53	2.0	1888	160	30.6
8	25.0	237.29	1.6	1971	204	26.0
19	50.0	92.90	1.9	2083	244	45.8
20	50.0	46.28	1.9	1913	244	64.9
7	75.0	228.43	1.4	1753	271	25.7
6	100.0	226.55	1.4	1583	291	24.4
15	100.0	87.26	1.5	2276	291	48.0
11	150.0	234.40	1.1	1747	322	28.3
21	150.0	94.52	1.3	1935	322	48.0
33	160.0	46.79	1.4	2080	327	68.0
22	200.0	230.10	1.2	1461	346	22.8
16	200.0	87.23	1.1	1711	346	46.5
30	200.0	45.75	1.2	1011	346	60.0
17	210.0	94.59	1.2	1307	350	43.3
25	1.0	236.11	1.3	2177	80	14.7
2	1.0	233.00	1.7	2157	80	15.0
12	1.0	237.97	1.8	2327	80	17.3
75	1.0	232.42	11.5	2002	80	26.3
77	1.0	232.31	11.0	2027	80	27.0
78	1.0	237.09	21.4	1977	80	40.0
76	1.0	229.26	22.7	1894	80	35.0
79	1.0	229.46	46.0	1896	80	58.1
1	1.0	95.81	2.0	2087	80	24.0
4	1.0	95.72	1.6	2409	80	28.7
26	1.0	46.57	2.3	2427	80	35.5
58	1.2	238.49	0.2	1922	85	8.3
42	1.2	234.47	2.0	2251	75	14.8
10	5.0	234.40	1.6	2125	132	23.0
68	10.0	219.48	1.4	2062	115	18.3
9	10.0	235.14	1.6	2133	160	25.6
5	50.0	229.43	1.6	1688	244	28.2
45	1.2	238.60	2.0	1317	13	4.2
46	1.2	237.20	2.0	2322	15	12.0
55	1.2	98.95	2.0	1522	17	9.0
63	1.2	45.37	0.2	1239	20	8.5
51	1.2	36.05	2.0	1542	17	13.7
50	1.2	39.40	2.0	1147	18	10.4
67	10.0	221.92	1.4	2051	70	15.1
69	10.0	93.30	1.6	1879	19	20.0
72	6.0	45.57	1.5	1548	1	20.6
66	10.0	228.00	1.2	2208	1	14.9
70	10.0	93.24	2.0	2048	1	22.4
73	30.0	46.03	2.0	1335	1	21.3
74	42.0	227.69	1.8	2011	1	15.4

Table 2
Model main results on TREPAM.

Test no.	$\delta_V(0)$ (μm)	$\delta_{Lm}(0)$ (μm)	$\delta_{Lt}(0)$ (μm)	$y_i(0)/r$	$y_m(0)/r$	$y_t(0)/r$	θ_{div} (rad.)	$q_{peak,exp}$ (MW m^{-2})	$q_{peak,th}$ (MW m^{-2})	$q_{peak,SI}$ (MW m^{-2})	$q_{peak,EH}$ (MW m^{-2})	e_{th} (%)	e_{SI} (%)	e_{EH} (%)
3	6.59	3.20	3.01	0.139	0.207	0.203	1.576	17.5	15.6	15.4	35.6	−10.91	−12.17	103.62
28	1.69	0.87	0.82	0.378	0.573	0.562	1.575	35.0	57.0		130.8	62.86		273.80
29	1.51	0.86	0.82	0.351	0.551	0.540	1.573	36.0	57.0		132.6	58.45		268.44
27	1.23	0.89	0.85	0.281	0.483	0.474	1.563	26.0	54.5		131.8	109.72		407.05
57	10.60	15.59	15.58	0.091	0.225	0.225	1.511	5.4	3.1	3.1	8.2	−42.72	−42.59	51.20
59	22.29	14.84	14.72	0.184	0.307	0.306	1.574	6.8	3.2	3.2	7.8	−52.59	−52.79	14.72
40	5.38	4.98	4.69	0.047	0.090	0.087	1.551	11.0	10.8	10.8	26.9	−1.76	−2.00	144.64
53	4.07	3.08	3.03	0.081	0.143	0.142	1.560	13.9	16.1	16.0	39.1	15.53	14.82	181.08
54	6.54	2.88	2.77	0.137	0.197	0.194	1.577	18.0	18.3	17.8	40.8	1.49	−1.11	126.60
61	15.68	6.07	6.05	0.673	0.933	0.932	1.581	16.0	7.6	7.3	16.5	−52.43	−54.56	3.15
60	7.51	6.76	6.74	0.316	0.601	0.600	1.552	8.7	7.0	7.0	17.2	−19.12	−19.43	97.90
62	9.11	5.59	6.46	0.405	0.653	0.692	1.579	6.0	3.8	3.8	9.0	−36.51	−37.33	49.52
48	3.48	1.85	1.78	0.185	0.284	0.280	1.576	24.0	28.7	28.4	65.9	19.51	18.17	174.74
36	2.05	2.13	2.15	0.088	0.179	0.180	1.540	16.1	21.8	21.7	55.4	35.11	34.66	244.26
65	6.83	4.56	4.60	0.583	0.971	0.975	1.567	14.5	9.8	9.8	23.4	−32.36	−32.76	61.31
64	3.25	4.86	5.02	0.273	0.681	0.694	1.500	10.9	8.7	8.7	23.0	−20.12	−20.37	111.35
71	3.82	2.38	3.02	0.081	0.131	0.145	1.574	30.6	32.9	32.1	75.2	7.43	4.97	145.67
8	5.98	3.85	5.47	0.050	0.083	0.097	1.576	26.0	23.8	22.9	55.6	−8.48	−11.77	113.68
19	3.24	2.06	3.17	0.070	0.114	0.138	1.669	45.8	51.6	47.8	116.0	12.60	4.45	153.22
20	2.03	1.47	2.27	0.088	0.151	0.186	1.559	64.9	68.7	65.8	163.6	5.86	1.39	152.13
7	4.30	3.72	6.02	0.038	0.070	0.090	1.513	25.7	28.0	26.9	69.6	9.07	4.59	170.67
6	3.53	3.66	6.12	0.031	0.064	0.085	1.437	24.4	28.3	27.2	74.5	15.85	11.60	205.33
15	3.47	2.09	3.46	0.080	0.127	0.159	1.601	48.0	57.5	52.9	125.9	19.77	10.23	162.28
11	4.37	4.01	6.96	0.037	0.071	0.097	1.470	28.3	28.3	26.7	72.4	0.14	−5.58	155.71
21	2.92	2.31	4.00	0.062	0.111	0.146	1.528	48.0	51.5	48.2	123.7	7.31	0.44	157.70
33	2.15	1.54	2.68	0.092	0.158	0.206	1.559	68.0	80.2	74.2	185.7	17.95	9.06	173.05
22	3.16	3.81	6.80	0.027	0.061	0.087	1.261	22.8	27.0	25.3	81.2	18.40	10.92	256.35
16	2.49	2.40	4.27	0.057	0.112	0.155	1.429	46.5	48.3	45.3	126.0	3.80	−2.49	170.87
30	0.87	1.77	3.18	0.038	0.115	0.177	1.773	60.0	72.8	71.1	183.0	21.33	18.57	204.93
17	1.75	2.46	4.43	0.037	0.089	0.131	1.032	43.3	34.9	30.7	128.1	−19.40	−29.10	195.82
25	16.14	5.59	5.18	0.137	0.184	0.181	1.582	14.7	9.4	9.1	19.9	−35.83	−38.23	35.66
2	13.83	4.86	4.51	0.119	0.160	0.157	1.581	15.0	10.8	10.4	22.9	−27.98	−30.60	52.47
12	15.18	4.71	4.35	0.128	0.167	0.164	1.584	17.3	11.5	10.9	23.5	−33.58	−36.94	35.84
75	4.75	1.89	1.77	0.041	0.057	0.056	1.578	26.3	27.1	26.4	59.3	3.06	0.53	125.44
77	4.94	1.93	1.80	0.043	0.059	0.058	1.579	27.0	26.7	26.0	58.0	−1.22	−3.89	114.86
78	3.45	1.40	1.31	0.029	0.041	0.040	1.578	40.0	36.4	35.5	80.1	−9.00	−11.18	100.23
76	3.08	1.35	1.26	0.027	0.039	0.038	1.577	35.0	37.4	36.7	83.4	6.94	4.86	138.36
79	2.17	0.95	0.89	0.019	0.027	0.027	1.577	58.1	53.3	52.3	119.0	−8.29	−10.07	104.75
1	7.78	2.89	2.69	0.162	0.223	0.219	1.580	24.0	18.0	17.4	38.5	−25.15	−27.50	60.37
4	10.73	3.15	2.90	0.224	0.290	0.285	1.586	28.7	17.5	16.5	35.2	−39.16	−42.68	22.50
26	6.31	1.83	1.68	0.271	0.350	0.343	1.586	35.5	30.2	28.4	60.3	−15.04	−20.03	69.95
58	32.59	14.39	13.81	0.273	0.394	0.389	1.585	8.3	3.7	3.6	8.2	−55.67	−56.51	−1.53
42	13.98	4.19	4.13	0.119	0.155	0.154	1.587	14.8	11.8	11.1	25.5	−20.57	−25.20	72.40
10	9.37	4.39	5.06	0.080	0.117	0.123	1.583	23.0	16.3	15.8	36.6	−28.98	−31.17	59.10
68	9.79	3.75	5.28	0.089	0.123	0.137	1.595	18.3	15.3	14.2	31.5	−16.49	−22.57	71.93
9	8.10	4.12	5.20	0.069	0.104	0.113	1.586	25.6	19.6	18.9	44.3	−23.47	−26.25	73.00
5	4.10	3.63	5.63	0.036	0.067	0.085	1.515	28.2	26.8	26.1	67.5	−5.11	−7.41	139.22
45	14.31	3.47	4.25	0.120	0.149	0.156	1.610	4.2	4.2	3.7	8.0	0.34	−13.10	90.67
46	23.52	3.29	3.94	0.198	0.226	0.232	1.629	12.0	8.5	9.1	15.1	−29.51	−24.33	25.53
55	10.04	2.24	2.70	0.203	0.248	0.257	1.611	9.0	8.0	6.8	14.7	−11.48	−24.11	63.40
63	16.75	4.96	5.99	0.738	0.957	1.002	1.600	8.5	3.1	2.8	5.8	−63.45	−66.94	−31.31
51	6.14	1.35	1.63	0.340	0.415	0.431	1.611	13.7	13.4	11.4	24.7	−2.26	−16.57	80.43
50	4.71	1.46	1.78	0.239	0.313	0.329	1.598	10.4	9.5	5.1	18.2	−8.26	−50.87	75.40
67	12.24	3.37	5.17	0.110	0.141	0.157	1.613	15.1	12.5	10.7	22.2	−16.96	−29.34	46.88
69	8.92	1.85	3.07	0.191	0.231	0.257	1.634	20.0	15.8	12.2	28.3	−21.23	−39.20	41.32
72	6.80	1.38	2.21	0.299	0.359	0.396	1.635	20.6	14.2	11.0	27.8	−31.22	−46.75	34.88
66	20.00	3.20	5.39	0.175	0.203	0.223	1.645	14.9	10.2	7.4	18.7	−31.23	−50.67	25.18
70	9.36	1.60	2.69	0.201	0.235	0.258	1.644	22.4	18.7	13.7	34.6	−16.30	−38.97	54.49
73	3.88	1.05	1.94	0.168	0.214	0.253	1.644	21.3	20.9	16.2	39.9	−1.74	−23.99	87.31
74	11.46	2.34	4.28	0.101	0.121	0.138	1.655	15.4	16.1	11.4	28.1	4.37	−26.30	82.37

sponding to the saturated [1] and the subcooled [2] cases. The calculated values $q_{peak,SI}$ given in Table 2 were obtained using the SI models, but instead of taking the fluid physical properties at T_{sat} as it is done in [1,2], the fluid physical properties were taken at $(T_\infty + T_{sat})/2$ for the liquid and at $(T_s + T_{sat})/2$ for the vapour. The second one is the model developed by Epstein & Hauser (EH model) in [5]. In their paper, a correlation for the Nusselt number Nu was derived from their model, from which $q_{peak,EH}$ is calculated and given in Table 2. We see that the present model and the SI model give very similar results for the tests with high subcooling and low superheat (case 1 tests), while for the tests with low subcooling and high superheat (intermediate and saturated cases), the SI model results diverge from the experimental results by underestimating the measured heat flux. This behaviour seems to confirm the importance of the inertia and convection terms in the vapour flow, which are considered in the present model but neglected in the SI model. These terms get progressively more important when the superheat is increased and the subcooling is decreased, and become predominant in the saturated tests, where the SI model gets the worst results. To have a more quantitative idea of the role

played by convection in the vapour flow, we may compare the superficial heat flux going from the surface to the vapour flow, q_{SV}, and the superficial heat flux going from the vapour flow to the interface, q_{VI} (if there is no convection, we have $q_{SV} = q_{VI}$). Calculated at the forward stagnation point, the previous heat fluxes are evaluated as follows:

$$q_{SV}(0) = -k_V \frac{\partial T_V}{\partial y}(0,0), \quad q_{VI}(0) = -k_V \frac{\partial T_V}{\partial y}(y_i,0)$$

In fact, the region of the forward stagnation point is the most interesting because it is the place where the convective effect on the heat transfer is maximal. This is because the front stagnation point is the place where the external tangential velocity gradient is maximal, and this velocity gradient is directly linked with the vapour velocity profile by Eq. (24) and the variable F_V. The higher the value of dU_e/dX and the higher the value of F_V and consequently, the values of the vapour tangential velocities. The relative importance of convection in the vapour flow is calculated by the "convection ratio" defined here by $(q_{SV}(0) - q_{VI}(0))/q_{SV}(0)$, which is given in Table 3 for each test. The calculated ratios confirm the previous analysis: while the ratio is close to 0% for case 1.1 tests, it progressively increases reaching values larger than 50% for the saturated tests.

As we can see in Table 2, the EH correlation largely overestimates the experimental heat fluxes, with errors of the order of 100%, and the results are worse when considering the high pressure tests with overestimations sometimes higher than 200%. The EH correlation calculated in Table 2 is in fact not based on an entirely analytical model but a corrected model in which a factor 2 was added in order to fit the experimental data of Motte and Bromley (MB) [6,7]. In part 4 some ideas will be developed to explain the divergence between the EH correlation, which works well on the MB experimental data, and the TREPAM experimental data.

3.3. Model analysis of the TREPAM tests

In this part, some additional results from the model are presented in order to analyse the TREPAM tests.

3.3.1. Variations of W_i, δ_V, δ_{Lm}, δ_{Lt} and $\dot{m}$ with θ

The variations of the five main variables with θ are analysed for the tests T40 and T45. These two tests are easily compared because they have almost the same wire diameter, water speed and pressure, but a different subcooling and superheat, meaning that T40 is a case 1 test and T45 an intermediate case test. Fig. 2(a) shows a typical variation of y_i, y_m, y_t with θ. In all tests, the three variables are almost constant in the front part of the cylinder, and begin to increase rapidly near the "equatorial" region ($\theta = \pi/2$). Depending on the case in which the test belongs, there are two kinds of behaviour when approaching the divergence point. In the "colder" tests (case 1.1 tests), $W_i \to 1$ before vapour flow separation occurs (see Fig. 2(b)): the liquid velocity profile becomes flat and consequently $\delta_{Lm} \to \infty$, but δ_V does not diverge. In the "hotter" tests (case 1.2, intermediate and case 2 tests), vapour flow separation occurs before $W_i \to 1$:$\delta_V \to \infty$ while δ_{Lm} does not diverge. In all cases, δ_{Lt} increases without diverging.

Some typical variations of the vapourisation rate $\dot{m}$ are shown in Fig. 2(c) for T40 and T45. In all tests, $\dot{m}$ is always maximum at $\theta = 0$ and decreases as θ increases. In the colder cases, $\dot{m}$ will decrease and eventually become negative, meaning that condensation occurs. In the hotter cases, $\dot{m}$ will decrease but remain positive even when reaching the vapour flow separation point, and consequently condensation will only take place in the vapour wake region. We may note a slight increase of $\dot{m}$ at the end of the calculation but this is due to the limitations of the present integral method: when using order 3 polynomials for the vapour temperature profile, the profile eventually becomes concave when approaching θ_{div}, as if there was some internal energy source in the vapour flow.

Table 3
Model analysis of TREPAM.

Test no.	$W_i(0)$	$W_{Vmax}(0)$	$A = Q_{JL}/Q_{vap}$	Convection ratio (%)	$q_{vap}(0)/q_{VI}(0)$ (%)
3	1.74	8.89	91.049	2.85	3.17
28	1.70	8.25	106.615	2.51	2.89
29	1.64	7.21	139.240	1.97	2.45
27	1.52	5.34	208.612	1.15	1.68
57	1.25	2.17	374.947	0.23	0.55
59	1.56	5.62	160.579	1.49	2.08
40	1.41	3.89	258.335	0.73	1.18
53	1.49	4.76	203.393	1.08	1.62
54	1.79	9.53	65.238	3.72	3.77
61	1.88	11.06	38.706	5.07	5.20
60	1.42	3.83	239.387	0.73	1.25
62	1.60	6.20	44.169	2.41	5.34
48	1.68	7.54	113.691	2.45	2.76
36	1.36	3.20	269.218	0.52	1.00
65	1.56	5.54	151.247	1.49	2.17
64	1.24	2.10	340.738	0.22	0.59
71	1.55	3.62	58.423	3.70	3.58
8	1.50	2.84	41.246	4.95	4.27
19	1.48	2.47	36.771	6.69	4.94
20	1.41	2.17	37.543	5.15	4.18
7	1.32	1.71	40.813	4.31	3.52
6	1.23	1.42	44.820	3.45	2.92
15	1.46	2.24	25.549	9.76	5.54
11	1.25	1.46	43.664	5.28	3.00
21	1.31	1.64	38.225	6.99	3.55
33	1.35	1.75	36.122	8.63	3.79
22	1.13	1.18	78.499	3.64	1.48
16	1.21	1.36	66.690	5.58	1.91
30	0.95	0.95	46.710	1.35	0.83
17	1.07	1.08	109.853	2.77	0.99
25	1.96	13.66	36.545	5.91	5.26
2	1.95	13.40	37.886	5.73	5.15
12	2.04	15.64	28.034	7.38	6.14
75	1.86	11.44	52.361	4.40	4.28
77	1.88	11.75	49.678	4.60	4.42
78	1.85	11.13	55.590	4.20	4.15
76	1.80	10.14	68.096	3.58	3.71
79	1.80	10.16	67.739	3.59	3.72
1	1.91	12.50	43.659	5.10	4.75
4	2.08	16.75	24.719	8.24	6.63
26	2.09	17.00	24.053	8.43	6.74
58	1.80	9.58	65.065	3.73	3.78
42	2.06	15.15	21.225	8.52	7.45
10	1.73	6.04	44.029	5.27	4.58
68	1.82	5.92	14.908	10.29	9.44
9	1.66	4.58	39.761	5.66	4.76
5	1.33	1.80	46.675	3.44	3.24
45	2.16	19.96	1.295	22.99	47.10
46	2.56	32.99	0.845	41.07	56.63
55	2.23	21.42	1.631	23.91	41.64
63	2.04	15.83	2.996	14.89	29.36
51	2.24	21.72	1.602	24.35	42.03
50	2.00	15.14	2.786	14.35	30.80
67	2.01	8.18	4.404	20.99	22.15
69	2.12	10.59	0.648	39.65	62.88
72	2.13	13.19	0.036	43.43	96.77
66	2.21	13.07	0.025	54.64	97.72
70	2.18	12.45	0.026	52.45	97.62
73	1.83	5.73	0.025	42.73	97.68
74	1.91	6.25	0.018	55.68	98.27

3.3.2. Velocity and temperature profiles

In almost all tests but T30, the calculated tangential velocity profiles are as shown in Fig. 3 at different angles for test T45. The vapour tangential velocity can be much higher than the liquid tangential velocity due to the pressure gradient induced by the external flow. Because the vapour density is much smaller than the liquid one, the vapour is accelerated to much higher speeds

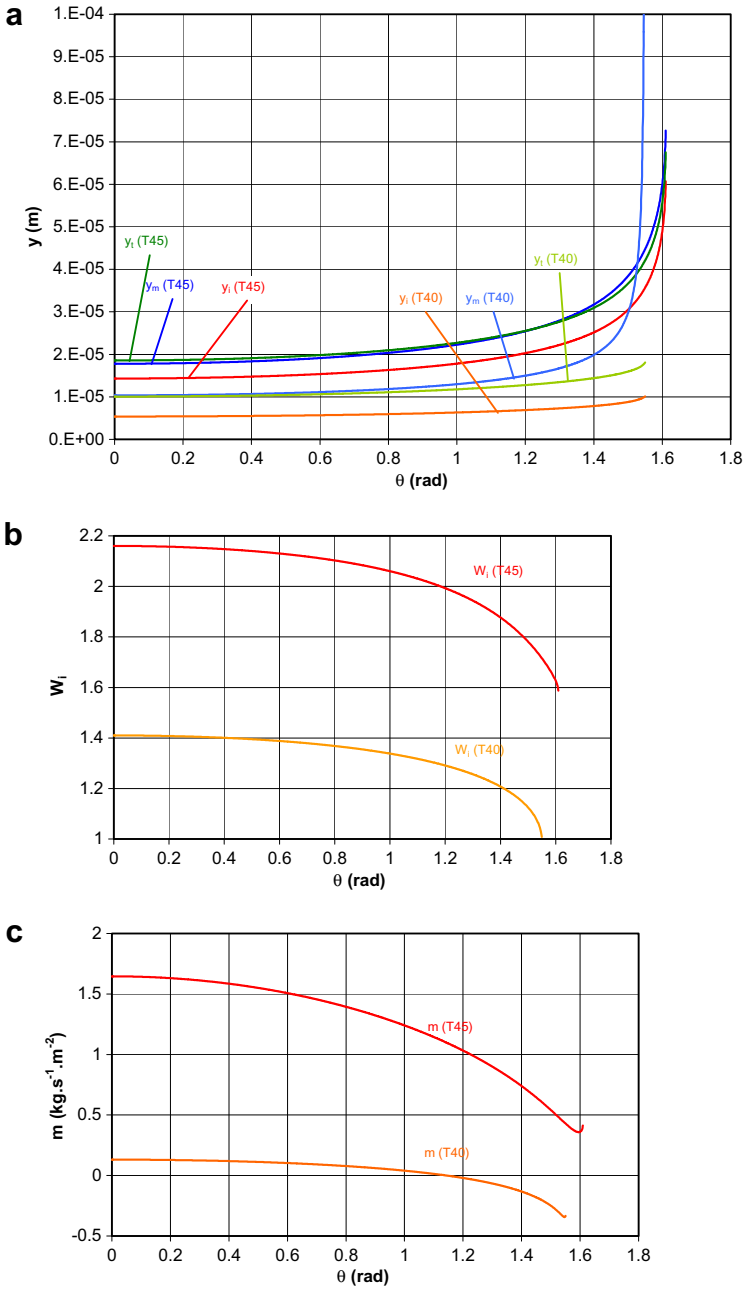

Fig. 2. Calculated variations of the five main variables with θ for tests T40 and T45. (a) y_i, y_m and y_t, (b) W_i and (c) $\dot{m}$.

for the same given pressure gradient. This is better visualised by considering the ratio of the vapour tangential velocity by the external tangential velocity, $W_V(y,x) = u_V(y,x)/u_e(x)$. For a given x, when y increases, W_V will increase until reaching a maximum value $W_{Vmax}(x) > 1$, and then decrease until it reaches the interfacial tangential velocity $W_i(x)$ (excepted for test T30). Because the external tangential velocity is maximum at the front stagnation point, the maximum value of W_{Vmax} is attained at $\theta = 0$, and also the maximum value of W_i. To have a global idea of the tangential velocity profiles in the TREPAM tests, the values of $W_{Vmax}(0)$ and $W_i(0)$ are given for all tests in Table 3. We see that two parameters may influence the values of $W_{Vmax}(0)$ and $W_i(0)$, which are the vapourisation rate and the pressure. At a given pressure, the hotter tests have the highest values of $W_{Vmax}(0)$ and $W_i(0)$. If the pressure increases, the values of $W_{Vmax}(0)$ and $W_i(0)$ will decrease, which is logical because the density ratio ρ_L/ρ_V decreases when the pressure increases. The extreme case is test T30 where $W_{Vmax}(0) = W_i(0) < 1$, meaning that the liquid moves faster than the vapour (the vapour is dragged by the liquid).

Typical temperature profiles are shown in Fig. 4, which illustrates two extreme cases in terms of convection ratio: T70 and T71. T71 has a convection ratio of only 3.7% which means that convection can be neglected in the vapour flow (see Table 3). Consequently, the temperature profile in the vapour film is almost linear on most of the cylinder surface, and becomes convex only when approaching the calculation divergence point. T70 has a convection ratio of 52.6% which means that convection in the vapour film plays a major role. Consequently, the curvature of the temperature profile in the vapour film is much more pronounced. The temperature profile remains almost unchanged when θ increases, and, as in the previous case, becomes convex only when approaching the calculation divergence point. This temperature profile variation with θ is observed in all

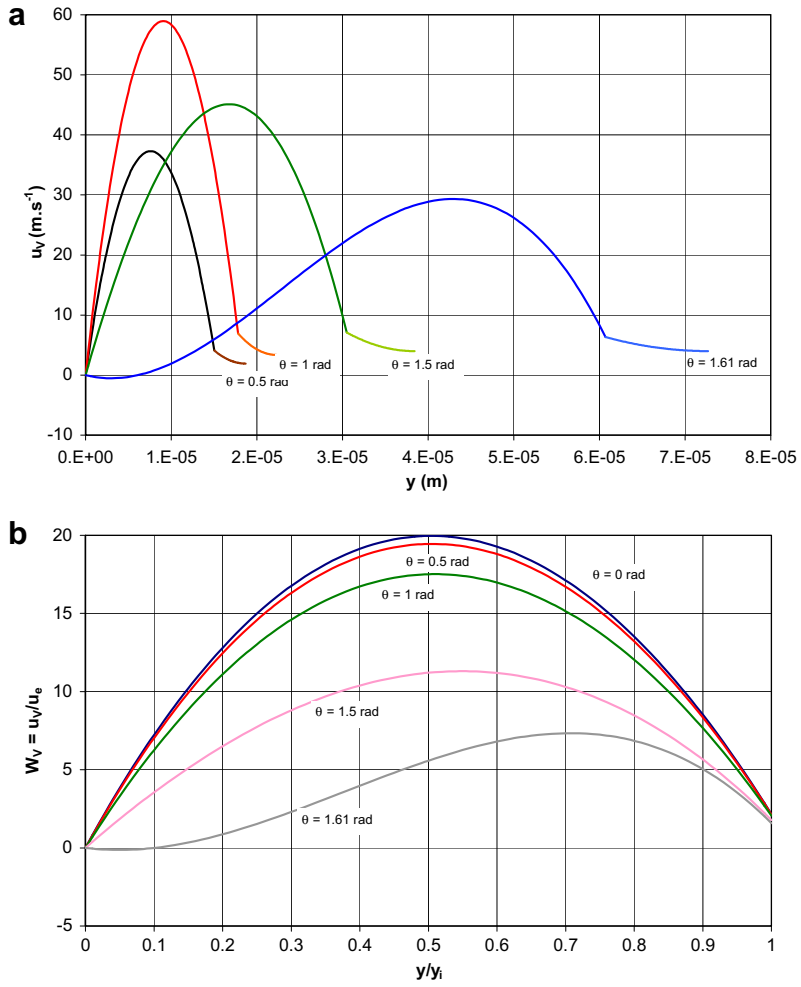

Fig. 3. Calculated tangential velocity profiles at different angles for test T45 from $\theta = 0$ to θ_{div}. (a) Dimensional velocity profiles for liquid and vapour and (b) dimensionless velocity profiles for vapour.

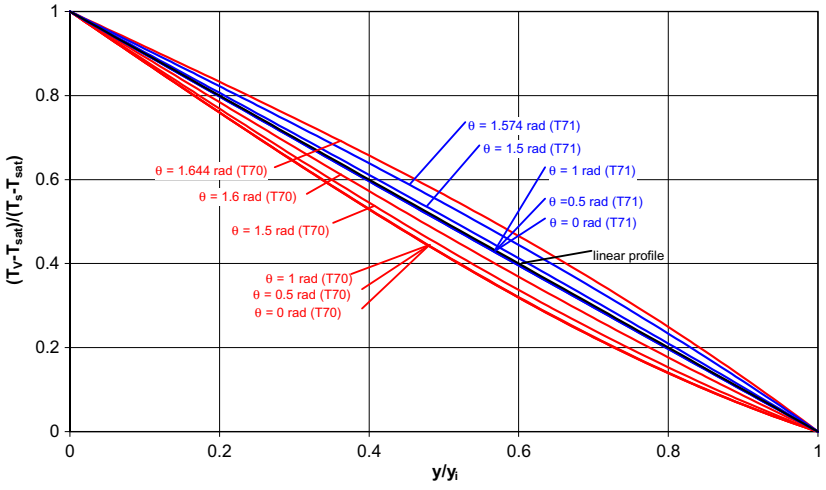

Fig. 4. Calculated vapour dimensionless temperature profiles from $\theta = 0$ to θ_{div} for tests T70 and T71.

other tests: the profile is first at its maximum positive curvature at $\theta = 0$ where the convection effects are stronger because of the maximum pressure gradient. Then, when θ increases, the curvature will continuously decrease until it becomes minimum and eventually negative when the calculation diverges.

3.3.3. Heat flux partition

In order to confirm the analysis undertaken in [4], the heat flux partition between liquid heating and liquid vapourisation was calculated for each test in Table 3. The partition is evaluated by calculating the ratio $A = Q_{IL}/Q_{vap}$ where:

$$Q_{IL} = \int_{\theta=0}^{\theta=\theta_{div}} -2rk_L \frac{\partial T_L}{\partial y}(y_i,\theta)d\theta = \int_{\theta=0}^{\theta=\theta_{div}} 2rq_{IL}(\theta)d\theta$$

$$Q_{vap} = \int_{\theta=0}^{\theta=\theta_{div}} 2rh_{LV}\dot{m}(\theta)d\theta = \int_{\theta=0}^{\theta=\theta_{div}} 2rq_{vap}(\theta)d\theta$$

q_{IL} and q_{vap} represent, respectively, the superficial heat flux going from the interface to the liquid and the superficial vapourisation heat flux. The calculated values of A confirm the previous analysis given in [4]. The case 1 test correspond to very high values of A where almost all the heat is used for liquid heating, while in the hotter tests identified as intermediate case tests we have $A \sim 1$. For the saturated case the value of A is in theory 0, but here A is just $\ll 1$ because the calculations have been done using $\Delta T_{sub} = 1$ K. Another way to estimate this heat partition is to compare q_{vap} with the superficial heat flux going from the vapour to the interface q_{VI} at the forward stagnation point. The calculated ratios $q_{vap}(0)/q_{VI}(0)$ are given in Table 3 for each test.

3.3.4. Analysis of the convective effect in other conditions than TREPAM

Some additional calculations have been done to analyse the effect of convection in conditions that have not been investigated in the TREPAM experiment. Particularly, there were very few saturated tests in TREPAM, so it appears interesting to calculate some virtual tests in additional saturated conditions. Therefore, two cases were investigated, one corresponding to saturated tests at $P_\infty = 1$ bar, and the other one corresponding to saturated tests at $P_\infty = 200$ bar. For each case, we calculated tests with $u_e = 1$ m s^{-1}, $d_0 = 1$ mm, and ΔT_{sup} from 500 to 3000 K. The wire diameter used is higher than the typical diameters in TREPAM in order to be sure that the boundary layer approximation is always valid. Each virtual test calculation is compared with calculations done using the SI model and a modified SI model which is based on the method described in [3] by Liu and Theofanous. This consists in considering the effects of convection by using the same SI model but with a modified latent heat which is called the effective latent heat and which is defined as $h'_{LV} = h_{LV} + 0.5C_{pV}\Delta T_{sup}$.

The resulting values for the mean heat fluxes are shown in Fig. 5(a). We see that the convective effect are much more important at the higher pressure of $P_\infty = 200$ bar. At the higher superheats, the heat fluxes calculated with the SI model are half of that calculated with the present model, and even for $\Delta T_{sup} = 500$ K the heat flux calculated by the SI model is already -30% of the present model value. For comparison, with $P_\infty = 1$ bar the value given by the SI model at $\Delta T_{sup} = 3000$ K is -31% of the value given by the present model.

The modified SI model succeeds in predicting the correct heat fluxes in both cases. The relative error with the present model is always less than 10%. It appears that this is an interesting method to predict heat fluxes even when the convective effects are very important. However, other important parameters will be predicted with less accuracy using this kind of method. An example of vapour film thickness calculations is shown in Fig. 5(b) to illustrate this. We see that in the $P_\infty = 200$ bar case, the vapour film thicknesses calculated from the modified SI model are quite different from those calculated with the present model. This is logical because the modified model uses a linear temperature profile instead of an order 3 profile which is concave, so a similar heat flux at the surface implies a smaller vapour thickness for the modified SI model. The calculated $\dot{m}(0)$ values shown in Fig. 5(c) are also quite interesting. We see that the SI model greatly overestimates the values of $\dot{m}(0)$ compared to the present model, with errors of more than 200%. The modified SI model performs much better, but still with errors between -25 and -30%.

4. Forced convection film boiling for "low" surface superheat

As already said, most of the previous convection film boiling experiments corresponded to relatively low surface superheat ($\Delta T_{sup} < 1000$ K for water). The present model, which is adapted to describe film boiling at higher superheat, works well on the TREPAM tests in which the lowest superheat is close to 1000 K, while correlations based on other existing models which were validated for lower superheat experiments fail to describe the TREPAM tests, as shown in [4]. However, these models were in fact corrected to match some experimental data: in the EH model, a factor 2 was added to match the Motte and Bromley experimental results, while in the Liu and Theofanous model [3], a turbulent eddy model describing the heat transfer at the wake region of the sphere needs to be added to the film boiling model at the front region of the sphere to match the experimental data. Curiously, for both experiments, the modelled heat coefficients based only on the film boiling models seem always to be much smaller (factor 2 of 3) than the experimental ones in the case of forced convection film boiling, while this do not happen to the present model when comparing to the TREPAM results. The answer may be given by analysing different quenching experiments of Honda et al. presented for example in [8,9]:

4.1. The Honda et al. quenching experiments results and analysis

The Honda et al. experiments are very similar to the TREPAM experiment, but cover different temperature and pressure ranges. They consist of the rapid quenching of preheated thin wires of 0.3 or 0.5 mm in diameter falling at a constant speed into a tank filled with water or ethanol at different temperatures. All tests were undertaken at ambient pressure and the initial wire temperatures were lower than those in TREPAM in the case of water (initial temperatures from 600 to 1400 °C). During the quenching, the temporal evolution of the wire temperature is continuously monitored, enabling the measurement of the instantaneous surface averaged heat flux evacuated from the wire, $q(t)$, as well as the instantaneous heat coefficient, $h(t) = q(t)/(T_s - T_{sat})$.

4.1.1. Observation of a different film boiling regime at low surface superheat

The boiling curves obtained from the wire cooling curves, as for example the ones shown in Fig. 6, cover different boiling regimes going from the film boiling to transient boiling and finally to the nucleate boiling regime at the lowest wire superheats. However, we see that these forced convection boiling curves are different from the classical pool boiling (or natural convection boiling) Nukiyama type curves that we would expect to obtain. If we take the boiling curve for the $\Delta T_{sub} = 50$ K test in Fig. 6(a), we observe the presence of two local minimum heat-flux points (MHF points), instead of only one that would be observed in a pool boiling curve. The first MHF point, referred as "M1" point, is located at a relatively high wire superheat. In Fig. 6(a), the M1 point is observed only for the tests with the lowest subcoolings. The second MHF point, referred as "M2" point, is observed in all tests and is located at a lower wire superheat. According to the authors, the M2 point corresponds to the classical transition point between film boiling and transition boiling but the M1 point corresponds to a transition between two different film boiling sub-regimes. When the wire superheat is higher than the M1 point superheat, we have a regime called the "stable film boiling" regime: a relatively thick vapour film entirely encloses the wire and a large wake is observed in its rear region. When the wire

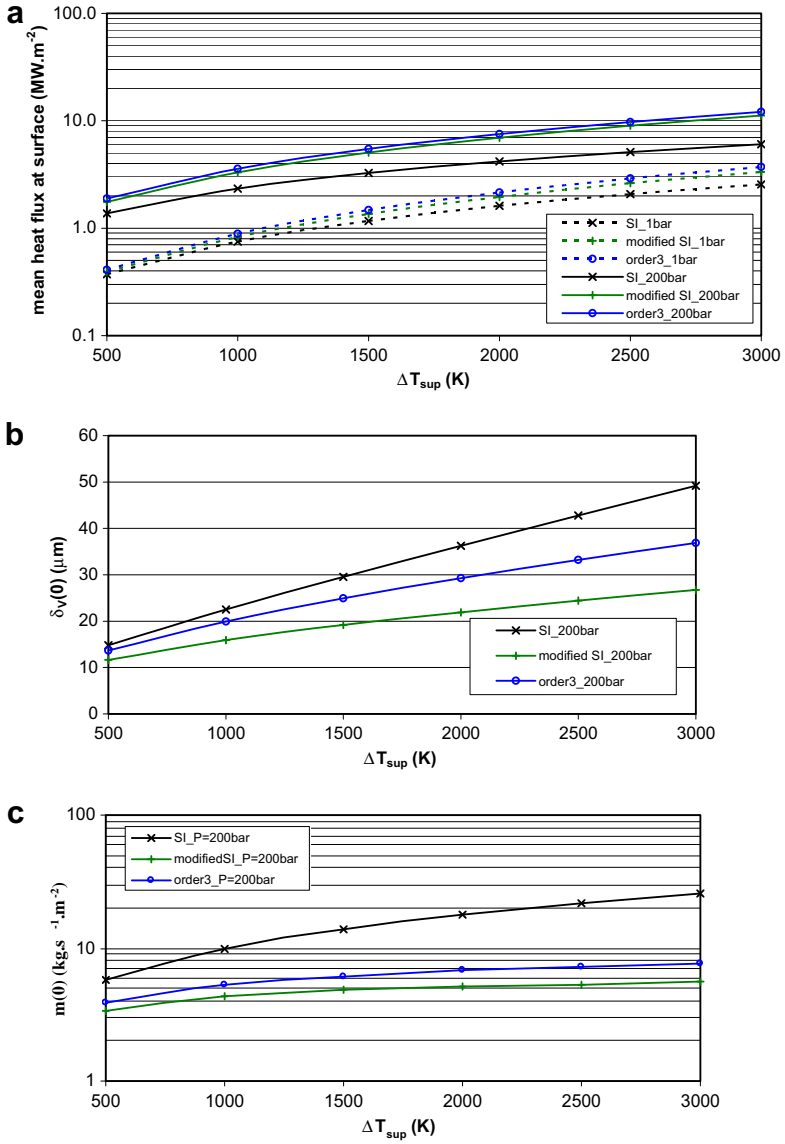

Fig. 5. Calculated surface heat fluxes (a), vapour film thicknesses at the front stagnation point (b), and $\dot{m}(0)$ values for some saturated cases at P_∞ = 1 bar and P_∞ = 200 bar, for ΔT_{sup} from 500 to 3000 K. The calculations have been done with d_0 = 1 mm, u_∞ = 1 m s^{-1} and ΔT_{sub} = 0.1 K, using the SI model, the modified SI model (with the use of the effective latent heat) and the present model which uses order 3 temperature and velocity profiles.

temperature decreases beyond the M1 point, we enter a regime called the "unstable film boiling" regime: according to the authors, the vapour film becomes unstable leading periodically to some liquid–solid contacts on the wire surface, a hypothesis which seems to be confirmed in [9] by electrically measuring these contacts.

The transition between the "stable" and "unstable" film boiling regimes is characterised by an important increase in the heat flux. If this transition is due to an instability growing on the vapour–liquid interface, this instability may induce liquid–solid contacts and/or lead to the formation of droplets entrained in this rear region. Both mechanisms will participate to an increased heat transfer: liquid–solid contacts enhances locally the heat transfer, while the droplets in the rear region will enhance the condensation of the vapour wake, thus increasing the heat transfer in the rear region which is usually neglected. In fact, a modification of the vapour wake is actually observed during the heat flux transition in [8]: according to the authors, the large vapour sheet which is observed in the "stable" film boiling regime seems to collapse when entering the "unstable" film boiling regime.

Some conclusions can be made by looking at the different quenching curves obtained in [8,9]. The "stable" low heat transfer regime seems to be favoured by high superheat, low subcooling, low velocities, and small diameters. For example, if we take a look at Fig. 6(a) and (b), we see that for a given wire diameter and speed, the M1 temperature decreases when the subcooling decreases. The influence of the diameter is seen when comparing Fig. 6(a) and (b): for a given speed and subcooling, the M1 point temperature is lower for the smallest diameter (d = 0.3 mm). And finally, the influence of liquid velocity is obvious when looking at Fig. 7(a). This behaviour seems coherent with the hypothesis that the low heat transfer region corresponds to stable film boiling. High superheat and low liquid subcooling produce thicker and therefore more stable vapour films. Decreasing the diameter has the effect of decreasing the distance an instability wave has to travel before reaching the vapour wake: if this distance is too small, the wave will "arrive" at the wake before it amplifies enough to approach the cylinder surface, thus mitigating the effect of instability in the heat transfer. And finally decreasing the liquid speed has the effect of decreasing the amplification rate of the instability.

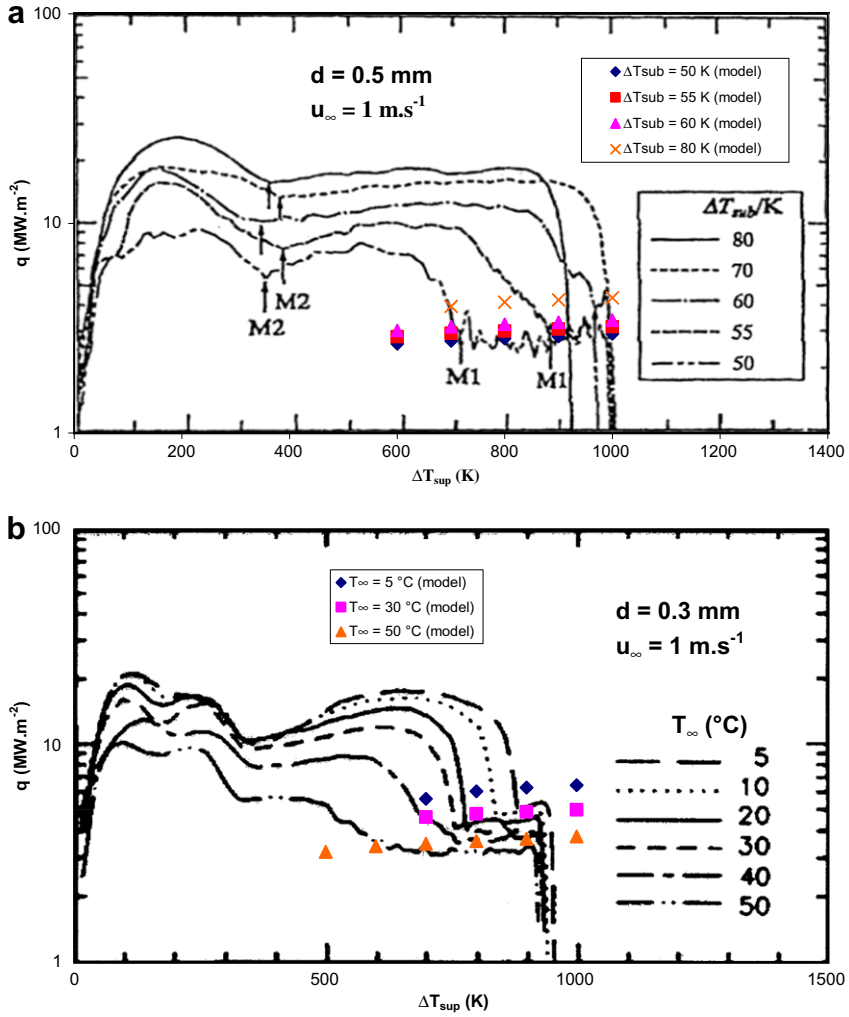

Fig. 6. Experimental heat transfer characteristics from [8,9] and model results for different water subcoolings and wire diameters. (a) $d = 0.5$ mm and (b) $d = 0.3$ mm.

4.1.2. Comparison of film boiling model results with the experimental data

The model results on the Honda data are shown in Figs. 6 and 7. The comparison with the experimental curves clearly shows that the model gets quite good results when predicting the heat flux in the "stable film boiling" regime, while it completely underestimates the heat flux (by a factor 2, 3 or more) in the "unstable" region. This behaviour seems coherent with the hypothesis of the existence of two film boiling sub-regimes. If a stable film boiling model is absolutely unable to predict the experimental results beyond the M1 point, another physical mechanism should be taking place there.

This may explain why in the EH model, a corrective factor of 2 is needed to fit the M&B experimental data which in fact did not always correspond to the stable film boiling regime (see Section 4.2). It may also explain why the Liu and Theofanous film boiling model described in [3] also underestimates the experimental heat fluxes by a factor 2 or 3 when the turbulent eddy model is not used (see Section 4.3). In fact, in those previous experiments, it was probably not possible to distinguish the two sub-regimes because almost all the experimental points corresponded to the unstable sub-regime. This can be understood by comparing Figs. 6(a) and (b): we see that if the diameter increases, the "stable" region reduces and eventually disappears for the large subcooling cases, which means that for a given liquid subcooling, increasing the diameter will increase the M1 point temperature. In the M&B and in the Liu experimental data, the cylinder or sphere dimensions are much larger than the Honda's wire diameter, so we can expect the M1 point to be located at very high surface temperatures which are beyond the maximum available experimental temperatures, even for a low liquid subcooling.

The decrease of q observed in Fig. 7(b) for the cases $u_\infty = 0.1$ and $0.2\ \mathrm{m\ s^{-1}}$ near $\Delta T_{sup} = 190$ K points out some limitations of the model which are caused by the quadratic velocity profiles used for the liquid phase. When decreasing the cylinder superheat from a high value, the dimensionless interfacial velocity at $\theta = 0$, $W_i(0)$ will decrease until it approaches 1. Because $W_i(\theta)$ decreases with θ from $\theta = 0$, the closer $W_i(0)$ is from 1, and the earlier the calculation will diverge when $W_i(\theta)$ gets equal to 1, which corresponds to a flat liquid velocity profile. Consequently, the calculated total heat transferred from the cylinder surface decreases (because heat transfer beyond θ_{div} is neglected) and therefore the surface averaged heat flux q also decreases. Then, beyond a critical value of ΔT_{sup} corresponding to $W_i(0) = 1$, we will have $W_i(0) < 1$, and no more divergence problems caused by the appearance of flat velocity profiles. As a consequence, the calculated value for q comes back to a "normal" value close to the experimental one. In the case of $u_\infty = 0.2\ \mathrm{m\ s^{-1}}$ for example, we have $W_i(0) \approx 1.00145$ for $\Delta T_{sup} = 191$ K: we get $\theta_{div} = 0.319$ rad. and $q \approx 0.131\ \mathrm{MW\ m^{-2}}$. But for $\Delta T_{sup} = 189$ K, we have $W_i(0) \approx 0.99987$: the calculation diverges only at $\theta = 1.872$ rad. when the vapour film separates and we get $q \approx 0.656\ \mathrm{MW\ m^{-2}}$.

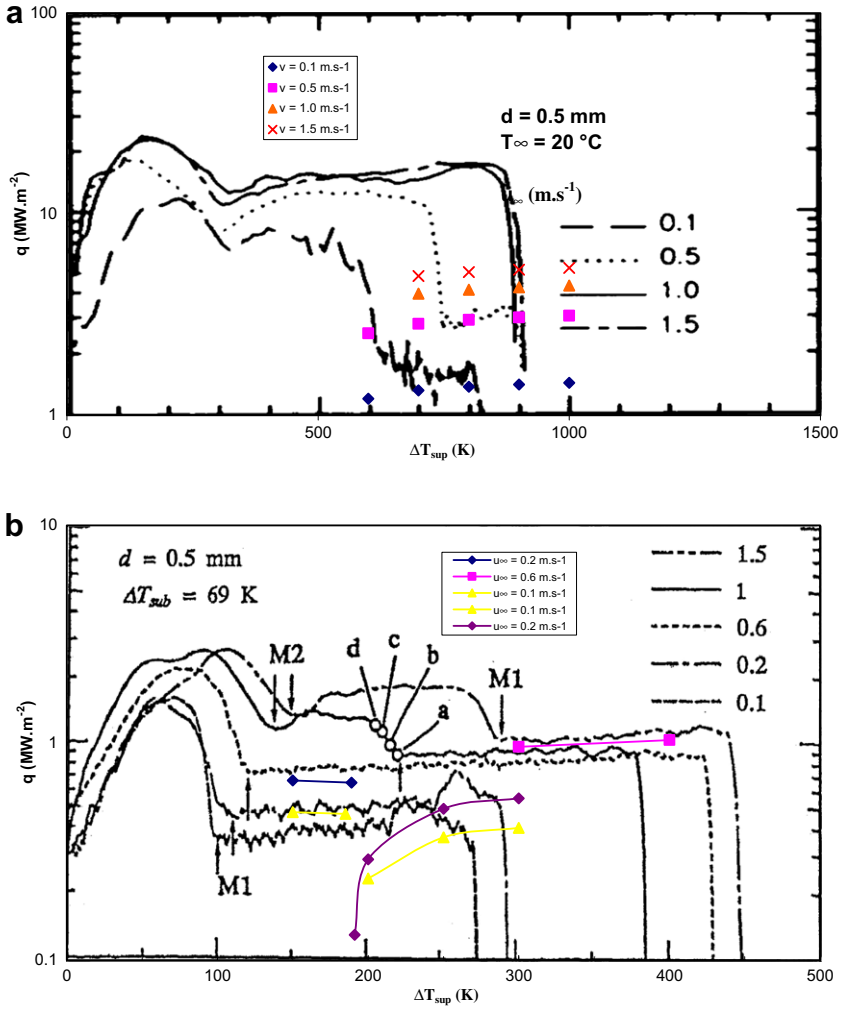

Fig. 7. Experimental heat transfer characteristics from [8,9] and model results for different wire speeds and fluids. (a) Water and (b) Ethanol.

4.2. Analysis of the Motte and Bromley experimental results

Motte and Bromley [6,7] undertook some convection film boiling experiments on horizontal cylinder using four different fluids: ethanol, hexane, carbon tetrachloride and benzene. Instead of observing the transient cooling of a preheated hot cylinder as in the previous experiments, the cylinder was continuously heated with a constant power supply. First, for a given flow velocity and temperature, the input power is increased until film boiling is reached and the cylinder temperature stabilizes. Then, when a steady state is reached, the heat flux evacuated from the cylinder is simply evaluated by measuring the power supplied to the cylinder. This method enables a direct evaluation of the heat flux q and the heat coefficient $h = q/(T_s - T_{sat})$ but it makes the observation of regime transitions more difficult because for a given fluid, diameter, liquid subcooling and liquid velocity there are at maximum three or four experimental points corresponding to different cylinder superheats.

In order to analyse the Motte and Bromley experimental data, all the experimental points where calculated using the present model. The test runs are organised as follows: for a given fluid, cylinder diameter and liquid subcooling, three or four tests corresponding to a "high", "medium" and "low" surface superheat are realised for a given speed, which usually is set to five different values going from approximately 1 to 4 m s^{-1}. Some results for ethanol with a 9.83 mm diameter cylinder are shown in Table 4 in which two experimental points series are represented, the first one (129–144) for a relatively high liquid subcooling and the second one (145–159) for a lower liquid subcooling. h_{exp} corresponds to the experimental value of the heat coefficient based on the power input at the cylinder, while h_{COexp} is the estimated value of the heat coefficient without radiation heat transfer. h_{COexp} is compared to the theoretical value h_{COth}, which is calculated using the present model. For the low subcooling series, we see that the model gets very good results, except for the low superheat tests at the higher speeds (152, 155 and 158). For the high subcooling series, the model underestimates h_{COexp} except for the higher superheat tests and the low speed tests.

These kinds of results are also observed for the other diameters and fluids and may be interpreted using the previous analysis of the Honda experiments. If there is a stable and an unstable film boiling regime, then for a given fluid, diameter, liquid subcooling, and liquid velocity, there should be a critical cylinder superheat (corresponding to a M1 point) beyond which, for a decreasing superheat, there should be a transition between a stable film boiling characterised by a relatively low heat transfer, and an unstable film boiling regime with a much higher heat transfer. If we look for example at tests 151–159, we see that for a given speed in which there are always three tests, the one corresponding to the lowest superheat has a h_{CO} which is always underestimated by the model. Therefore, these tests are probably in the unstable regime zone, while the others are in the stable one. Furthermore, it is possible

Table 4
Model results for ethanol on some experimental points from Motte [9]. The highlighted lines correspond to tests in which is model prediction for h_{CO} is less than 65% of the experimental value. These tests are probably in the unstable film boiling regime.

Test no.	u_∞ (m s^{-1})	ΔT_{sup} (K)	ΔT_{sub} (K)	h_{exp} (W m^{-2} K^{-1})	h_{COexp} (W m^{-2} K^{-1})	h_{COth} (W m^{-2} K^{-1})	$(h_{COth} - h_{COexp})/h_{COexp}$ (%)
129	1.11	841	44.7	647.9	552.5	476.0	−13.85
130	1.11	428	44.6	1411.1	1378.2	549.4	−60.14
131	1.11	1001	43.7	777.4	642.8	492.0	−23.46
132	1.53	897	43.2	824.0	716.1	558.9	−21.95
133	1.53	412	43.8	1260.6	1228.8	649.3	−47.16
134	1.53	971	42.7	863.7	738.8	568.2	−23.09
135	2.45	624	42.8	1726.3	1668.9	693.1	−58.47
136	2.45	402	42.4	1987.5	1956.8	816.0	−58.30
137	2.45	1123	41.2	1013.1	956.3	747.9	−21.79
138	3.33	549	40.4	1984.7	1938.1	808.0	−58.31
139	3.33	439	41.3	2112.4	2078.4	888.1	−57.27
140	3.33	1204	39.8	1113.6	920.5	891.6	−3.14
141	4.19	600	38.6	2240.2	2186.3	877.3	−59.87
142	1.10	409	44.1	983.0	951.7	557.4	−41.44
143	4.17	495	40.5	2412.8	2372.5	932.8	−60.68
144	4.17	917	38.4	1805.8	1693.9	905.7	−46.53
145	1.07	670	12.6	491.8	427.0	379.4	−11.16
146	1.07	462	12.9	484.4	441.8	354.8	−19.69
147	1.07	831	12.3	525.8	432.7	406.4	−6.08
148	1.54	668	11.6	551.4	487.8	449.4	−7.87
149	1.54	440	11.4	545.1	511.1	415.0	−18.80
150	1.54	871	11.2	646.2	544.6	491.0	−9.85
151	2.07	616	11.8	800.7	745.0	510.6	−31.47
152	2.07	402	12.1	857.5	826.8	482.1	−41.70
153	2.07	885	11.1	675.8	570.7	572.6	0.33
154	3.35	702	11.5	918.8	849.5	671.1	−21.00
155	3.35	421	12.7	1175.5	1142.0	617.9	−45.90
156	3.35	885	12.1	981.3	933.0	729.6	−21.80
157	4.20	722	11.5	1097.7	1025.0	757.6	−26.09
158	4.20	396	11.7	1555.9	1525.8	682.1	−55.30
159	4.20	898	11.3	1120.4	1012.5	819.2	−19.09

to qualitatively say if a test is in the stable or the unstable region by comparing h_{COexp} and h_{COth}. For example, if h_{COth} is less than −35% of h_{COexp}, the test is said to be in the unstable region. The result obtained by undertaking this analysis is coherent with the hypothesis of the existence of the two regimes in film boiling: in the previous analysis of Honda's experiments, it was observed that the M1 point corresponding superheat, ΔT_{sup}(M1), increases when the speed, the liquid subcooling and the diameter increases, and this is qualitatively observed in Table 4. The effect of the liquid subcooling is quite clear: for a given speed, increasing the liquid subcooling will increase the M1 point superheat. For example, for $u_\infty \approx 1$ m s^{-1} or $u_\infty \approx 1.5$ m s^{-1}, tests with $\Delta T_{sup} \approx 430$ K are "stable" if the liquid subcooling is low and "unstable" for a higher subcooling. For $u_\infty \approx 4.2$ m s^{-1}, all the highly subcooled tests are "unstable" while for comparable values of ΔT_{sup}, only test 158 is "unstable" for the tests with low subcooling. The effect of speed is also observable when comparing tests 129–131 and tests 141, 143–144. At $u_\infty \sim$ 4.2 m s^{-1}, test 144 with $\Delta T_{sup} = 917$ K is still in the unstable regime while at $u_\infty \sim 1.1$ m s^{-1}, test 129 with $\Delta T_{sup} = 841$ K is in the stable regime. Finally, the effect of diameter is in fact quite important if we compare the present experiment with the Honda's tests. In Fig. 8 of [9], it is reported for ethanol that for a speed of 1 m s^{-1}, wire diameters of 0.3 or 0.5 mm and liquid subcoolings of 40–50 K, the value of ΔT_{sub}(M1) is approximately 120 K. Comparatively, test 130, which corresponds to the same speed, the same liquid subcooling, but a cylinder diameter of 9.83 mm, is in the unstable regime with $\Delta T_{sup} = 428$ K, which means that ΔT_{sup}(M1) > 428 K.

All the previous analysis is also valid for the other experimental points corresponding to the other diameters and fluids: for a given speed, diameter and subcooling, the model gives excellent results when ΔT_{sup} is higher than a critical value ΔT_{sup}(M1), but underestimates the heat transfer when $\Delta T_{sup} < \Delta T_{sup}$(M1). The value of ΔT_{sup}(M1) seems to increase when the speed, the subcooling and the diameter increases. Of course, this is just a qualitative analysis, because there are too few experimental points for different values of ΔT_{sup} in order to precisely evaluate ΔT_{sub}(M1) each time, but nevertheless the same tendencies as shown in Table 4 are observed for the four fluids. It is also to be noted that when the model predicts the heat coefficient in the stable film boiling regime, the relative error is almost always negative: the model slightly underestimates the heat transfer, which is coherent with the model approximation of neglecting heat transfer at the rear region of the cylinder.

In conclusion for this part, we can say that the Motte and Bromley tests cover in fact two different film boiling regimes, and this must be taken into consideration when using these experimental points for correlations. And while there are no models capable of predicting the heat transfer in the unstable film boiling regime, it is at least possible, as shown in this simple example using Table 4, to say qualitatively to which sub-regime belongs an experimental point using an accurate stable film boiling model.

4.3. Liu turbulent eddy model in the case of film boiling on spheres

According to Liu and Theofanous in [3], the divergence between their film boiling model and their experimental results in the case of subcooled forced convection is due to the omission of the heat transfer and the rear of the sphere. Therefore, they proposed a turbulent eddy model to calculate the heat flux at the rear of the sphere. This model is based on a previous model developed by Theofanous to study turbulent mass transfer at a free gas–liquid interface. Based from this model, the calculated local heat flux density at the rear of the sphere is given the following expression:

$$q_{SV} = 0.25\Delta T_{sub}\rho_L C_{pL} Pr_L^{-1/2}(4\nu_L^2 c^6 g^3 d)^{1/8}(Fr/2)^{n_1} \quad (58)$$

(Fr is defined using the sphere radius). q_{SV} is constant from $\theta = \theta_{div}$ to $\theta = 180°$. By matching this expression with the experimental data, the values $c = 0.27$ and $n_1 = 0.45$ were used. Eq. (58) is valid only

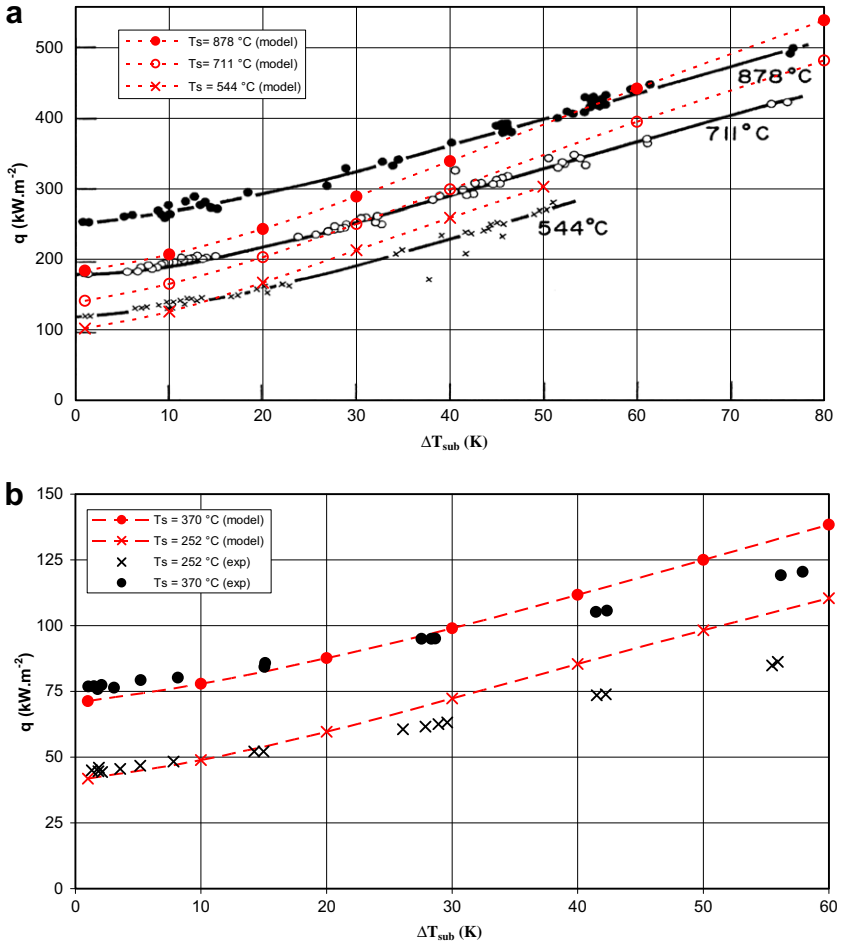

Fig. 8. Model results on the experimental data of Ede and Siviour [14]. (a) 3.17 mm diameter cylinder in water and (b) 3.17 mm diameter cylinder in ethanol.

for $Fr \geqslant 12$. For $4/9 < Fr < 12$, which corresponds to mixed convection, q_{SV} is calculated by:

$$q_{SV} = q_{SV,Fr=12}\left(\frac{Fr}{12}\right)^{n_2} \tag{59}$$

By matching (59) with the experimental data, a value of 3/4 is found for n_2.

When including the contribution of the rear of the sphere in the heat transfer using (58) or (59), the agreement with the experimental data is much better. In general, by using this model, the heat evacuated from the rear is approximately the same as the front contribution. The major drawback of this model is that it does not predict any sharp transition from a "low" to a "high" heat flux regime: the calculated values of q_{SV} at the rear are independent of the sphere superheat. So an additional physical mechanism is still needed to explain this transition. There is unfortunately no experimental evidence of this transition in the spherical case, although it would be quite surprising that convection film boiling on a sphere will differ from the horizontal cylinder in a way such that this transition would not exist. As it was said before, the sphere diameters in [3] (from 6.35 to 19.1 mm) are such that all the tests are probably within the unstable regime.

4.4. Conclusion

The analysis of the previous experiments shows that the experimental and theoretical analysis of forced convection film boiling is not straightforward because of the existence of two different sub-regimes, referred here as the "stable" and "unstable" film boiling sub-regimes, which led to some confusion when analysing the experimental data. The main reason for that is that in some experiments only one sub-regime is observable: for example, the sub-cooled forced convection experiments on spheres of Liu seem to be exclusively in the "unstable" sub-regime while only the "stable" sub-regime is observable in TREPAM.

The analysis of the experimental results of Honda et al. led to the conclusion that the appearance of the different sub-regimes seems closely linked to the stability of the vapour film during film boiling: the "unstable" sub-regimes corresponds to liquid–solid contact which can be measured, and the influence of the different experimental parameters on the occurrence of the different sub-regimes seems also very coherent with the stability hypothesis. The additional analysis given here with the present model seems to confirm this hypothesis: the heat transfer in "stable" film boiling can be accurately predicted with the present "stable" film boiling model, but is largely underestimated in "unstable" film boiling.

The next step for forced convection film boiling modelling should be the prediction of the occurrence of "unstable" and "stable" sub-regimes, using for example a stability analysis. Some work has already been done by Honda et al. for cylinders in [10,11], and for spheres in [12], but additional work is needed in order to predicted more accurately the frontiers between the two sub-regimes.

5. Free convection film boiling

The last case to be analysed is the one corresponding to pool film boiling type experiments, which is the limiting case when the external flow speed is zero. As it was pointed out in the previous part, it seems there is an important difference with forced convection: the film boiling regime in forced convection is subdivided into two sub-regimes of stable and unstable film boiling, while this is not noticeable in pool film boiling when observing for example a classical Nukiyama type curve. The experimental results of Honda and Bromley have also pointed out the fact that the unstable film boiling regime tends to progressively disappear when the external flow speed is decreased (see Fig. 7(b)): for a given liquid subcooling and cylinder diameter, the M1 point temperature decreases when the speed decreases, and eventually approaches the M2 point temperature, which means that there is ultimately a direct transition between stable film boiling and transition boiling. This is coherent with the fact that in the limiting case of free convection, no unstable film boiling regime is observed.

In fact, liquid–solid contacts do actually exist in saturated or low subcooling pool film boiling, as shown for example in [13], but they are believed to have a negligible effect on the global heat transfer, which means that pool film boiling can be studied with a stable film boiling model. Therefore, the present model was used to calculate some pool boiling experimental points. In practice, because the speed cannot be set exactly to zero, the speed is set to a "small" value which corresponds to a very small value of the Froude number, beyond which the calculations results do not change.

The experimental data of Ede and Siviour [14] was analysed with the present model. In this experiment, the pool film boiling of cylinders of different diameters in water and ethanol was investigated. In all cases, the model results were quite good, with relative errors always less than 30%. A typical result is shown in Fig. 8. We observe that while the agreement is quite good, the model seems always to overestimate the variation of the heat flux with the amount of subcooling: the model underestimates the heat flux in saturated pool film boiling but overestimates it in the case of important subcooling. The reason for this behaviour is not very clear. For saturated or low subcoolings, the model underestimates the heat transfer, but contrary to the case of forced convection film boiling, this cannot be accounted to the omission of the heat transfer in the back of the cylinder because in the case of pool film boiling the calculated divergence point is almost π. The underestimation of the heat transfer observed for example for water with a 878 °C cylinder may come from the fact that the vapour interface is very irregular in the case of saturated or low subcooling, as observed in [13]. It is also to be noted that this is only a 2D model while in reality the pool film boiling flow may be 3D depending on the ratio between a characteristic wavelength from Rayleigh–Taylor instabilities that would appear in the back of the cylinder at the liquid vapour interface and the cylinder diameter.

6. Conclusion

A film boiling model based on a classical boundary layer approach has been developed to study the forced, mixed and free convection film boiling on a horizontal cylinder in a saturated or subcooled liquid. The main feature of the model is to include the convection and the inertia terms in the vapour flow equations, which effects become important in the case of a highly superheated surface. This addition is found to be useful when comparing the model results with the experimental results of TREPAM, an experimental device dedicated to study the quenching of thin wires at very high temperatures. This model was also compared to a simpler model which does not include these terms in order to have a more quantitative idea of their effects in the heat transfers.

The model was then compared with experimental data corresponding to low superheat and high subcooling in the case of forced convection, but, as for the previous film boiling models, it did not succeed in predicting the heat transfers in some cases. The reason for that was carefully investigated and it was concluded that there are in fact two different film boiling sub-regimes, one corresponding to relatively low heat transfers at the higher superheats and another one corresponding to much higher heat transfers which appears at lower superheats. The transition between these two regimes can be very sharp. The existence of these two sub-regimes is probably linked with the vapour film stability and therefore to the possibility of liquid–solid contacts occurring within the film boiling regime which may explain the sharp increase of the heat transfer. This is quite different from free convection film boiling case, where there are no such sub-regimes.

In the case of high temperature film boiling, further improvement is needed in the present model in order to include radiation heat transfer which becomes very important when studying film boiling on high temperature and high emissivity surfaces. But the case of low superheat and high subcooling shows that the even the basic physical phenomena need still to be understood in that case. An additional approach, different from the classical film boiling models, is needed to include for example liquid–solid contacts or to describe the heat transfer at the wake region.

References

[1] T. Ito, K. Nishikawa, T. Shigeshi, Forced convection film boiling heat transfer from a horizontal cylinder to liquid cross-flowing upward (1st Report, saturated liquid), Bulletin of JSME 24 (198) (1981).
[2] T. Shigeshi, T. Ito, K. Nishikawa, Forced convection film boiling heat transfer from a horizontal cylinder to liquid cross-flowing upward (2nd Report, subcooled liquid), Bulletin of JSME 26 (214) (1983).
[3] C. Liu, Film boiling on spheres in single and two phase flows, Ph.D. Thesis, University of California, Santa Barbara, 1994.
[4] G. Berthoud, L. Gros d'Aillon, Quenching of a very high temperature thin wire immersed into water at pressure from 1 to 210 bars, International Journal of Thermal Sciences (in press).
[5] M. Epstein, G.M. Hauser, Subcooled forced-convection film boiling in the forward stagnation region of a sphere or cylinder, International Journal of Heat and Mass Transfer 23 (1980) 179–189.
[6] E.I. Motte, Film boiling of flowing subcooled liquids, M.S. Thesis, University of California, Berkley, 1954.
[7] E.I. Motte, L.A. Bromley, Film boiling of flowing subcooled liquids, Industrial and Engineering Chemistry 49 (1957).
[8] H. Honda, H. Takamatsu, H. Yamashiro, S. Kobayashi, Heat transfer characteristics during rapid quenching of a thin wire in water, Heat Transfer – Japanese Research 21 (8) (1992).
[9] H. Honda, H. Takamatsu, H. Yamashiro, Minimum heat-flux point and liquid solid contact during rapid quenching of thin wires, Heat transfer – Japanese Research 24 (6) (1995).
[10] H. Yamashiro, H. Takamatsu, H. Honda, Theoretical analysis of the stability of vapor film in subcooled film boiling on a horizontal wire, Heat Transfer – Japanese Research 26 (4) (1997).
[11] H. Honda, H. Takamatsu, H. Yamashiro, Stability of vapor film in subcooled forced convection film boiling on a horizontal cylinder (an analysis considering the effect of periodic heat conduction), Transactions of the Japan Society of Mechanical Engineers – B 64 (628) (1998) 4166–4171.
[12] H. Honda, O. Makishi, H. Yamashiro, Generalized stability theory of vapor film in subcooled film boiling on a sphere, International Journal of Heat and Mass Transfer 50 (2007) 3390–3400.
[13] Y. Kikuchi, T. Ebisu, I. Michiyoshi, Measurement of liquid–solid contact in film boiling, International Journal of Heat and Mass Transfer 35 (6) (1992) 1589–1594.
[14] A.J. Ede, J.B. Siviour, Sub-cooled film boiling on horizontal cylinders, International Journal of Heat and Mass Transfer 18 (1975) 737–742.
[15] K. Nishikawa, T. Ito, T. Kuroki, K. Matsumoto, Pool film boiling heat transfer from a horizontal cylinder to saturated liquids, International Journal of Heat and Mass Transfer 15 (4) (1972) 853–862.
[16] K. Hama, M. Shiotsu, Film boiling on a vertical plate in subcooled helium II, Cryogenics 47 (4) (2007) 209–219.